

AD 734044

THE SCATTERING FROM ROUGH CURVED SURFACES OF A WAVE PROPAGATED THROUGH A RANDOM MEDIUM

By

Darryl P. Greenwood and E. J. Powers
Department of Electrical Engineering

Technical Report No. 104
June 1, 1971

DDC
RECEIVED
DEC 17 1971
B

PLASMA AND QUANTUM ELECTRONICS RESEARCH LABORTORY

Reproduced by
NATIONAL TECHNICAL
INFORMATION SERVICE
Springfield, Va. 22151

ELECTRONICS RESEARCH CENTER
THE UNIVERSITY OF TEXAS AT AUSTIN

Austin, Texas 78712
Approved for public release;
distribution unlimited.

89

The Electronics Research Center at The University of Texas at Austin constitutes interdisciplinary laboratories in which graduate faculty members and graduate candidates from numerous academic disciplines conduct research.

Research conducted for this technical report was supported in part by the Department of Defense's JOINT SERVICES ELECTRONICS PROGRAM (JSEP), U.S. Army, U.S. Navy, and the U.S. Air Force through the Research Contract (JCSE) F44670-71-C-0091. This program is monitored by the Department of Defense's JSEP Technical Advisory Committee consisting of representatives from the U.S. Army Electronics Command, U.S. Army Research Office, Office of Naval Research, and the U.S. Air Force Office of Scientific Research.

Additional support of specific projects by other Federal Agencies, Foundations, and The University of Texas at Austin is acknowledged as indicated to the appropriate sections.

Reproduction, translation, publication, use and disposal in whole or in part by or for the United States Government is permitted.

Qualified requestors may obtain additional copies from the Defense Documentation Center; all others should apply to the Clearinghouse for Federal Scientific and Technical Information.

ADDITIONAL		
CH21	WHITE SECTION	<input checked="" type="checkbox"/>
408	GRAY SECTION	<input type="checkbox"/>
674000000		<input type="checkbox"/>
MULTI-COPY		
BY		
DISTRIBUTION/AVAILABILITY CODES		
INT.	AVAIL.	AND/OR SPECIAL
A		

UNCLASSIFIED

Security Classification

DOCUMENT CONTROL DATA - R&D		
(Security classification of title, body of abstract and indexing annotation must be entered when the overall report is classified)		
1. ORIGINATING ACTIVITY (Corporate author) The University of Texas at Austin Electronics Research Center Austin, Texas 78712		2a. REPORT SECURITY CLASSIFICATION UNCLASSIFIED
		2b. GROUP
3. REPORT TITLE THE SCATTERING FROM ROUGH CURVED SURFACES OF A WAVE PROPAGATED THROUGH A RANDOM MEDIUM		
4. DESCRIPTIVE NOTES (Type of report and inclusive dates) Scientific Interim		
5. AUTHOR(S) (Last name, first name, initial) Darryl P. Greenwood E. J. Powers, Jr.		
6. REPORT DATE 1 June 1971	7a. TOTAL NO. OF PAGES 94	7b. NO. OF REFS 19
8a. CONTRACT OR GRANT NO. F44620-71-C-0091	8b. ORIGINATOR'S REPORT NUMBER(S) JSEP, Technical Report No. 104	
a. PROJECT NO. 4751		
c. 61102F	9b. OTHER REPORT NO(S) (Any other numbers that may be assigned this report) AFOSR-TR-71-1988	
d. 681305		
10. AVAILABILITY/LIMITATION NOTICES 1. This document has been approved for public release and sale; its distribution is unlimited.		
11. SUPPLEMENTARY NOTES TECH, OTHER	12. SPONSORING MILITARY ACTIVITY JSEP through AF Office of Scientific Research (NE) 1400 Wilson Boulevard Arlington, Virginia 22209	
13. ABSTRACT <p>A generalized investigation of wave scattering from rough surfaces yields an expression for mean scattered power flux which is the spatial Fourier transform of the product of three transfer functions: (a) the optical transfer function (OTF) of the propagating medium, (b) the joint characteristic function of the surface roughness, and (c) a coherence involving the mean surface and the wave profile. The results are applicable to rough surfaces which do not have rms slopes greater than a few degrees.</p> <p>The solution is applied to laser scattering from aluminum and titanium airplane surfaces where the medium is the clear atmosphere. Proficorder tracing of sample rough surfaces reveals independent "roughness" and "waviness" components normally distributed with Gaussian (isotropic) auto-correlation. The deterministic surface model is a generalized quadratic approximation to the surface mean. The laser profile is the lowest-order circular laser mode. The atmospheric OTF is modeled as Gaussian.</p> <p>For typical parameters, the result decouples into a specular term (depending on turbulence, wave profile, and the known surface) and a diffuse component (depending on the rough and known surfaces). The deterministic surface is deformed spherically to account for an incident wave of slight spherical character. (A spherical wave affects only the coherent scatter.) From a measurement of scatter at normal incidence the surface power spectral density and the atmospheric refractive index structure constant may be determined provided the surface is isotropic, homogeneous, and normally distributed.</p> <p>Rough surface and profile aspects of the theory are verified by nearfield measurements of scatter from titanium and aluminum when there is no turbulence present. Surface power spectral densities found empirically from scatter at normal incidence agree with the spectra found from proficorder tracing.</p>		

DD FORM 1473

JAN 64

UNCLASSIFIED
Security Classification

UNCLASSIFIED
Security Classification

14 KEY WORDS	LINK A		LINK B		LINK C	
	ROLE	WT	ROLE	WT	ROLE	WT
ATMOSPHERE						
DIFFRACTION						
ELECTROMAGNETIC						
LASERS						
TURBULENT						

INSTRUCTIONS

1. ORIGINATING ACTIVITY: Enter the name and address of the contractor, subcontractor, grantee, Department of Defense activity or other organization (*corporate author*) issuing the report.

2a. REPORT SECURITY CLASSIFICATION: Enter the overall security classification of the report. Indicate whether "Restricted Data" is included. Marking is to be in accordance with appropriate security regulations.

2b. GROUP: Automatic downgrading is specified in DoD Directive 5200.10 and Armed Forces Industrial Manual. Enter the group number. Also, when applicable, show that optional markings have been used for Group 3 and Group 4 as authorized.

3. REPORT TITLE: Enter the complete report title in all capital letters. Titles in all cases should be unclassified. If a meaningful title cannot be selected without classification, show title classification in all capitals in parenthesis immediately following the title.

4. DESCRIPTIVE NOTES: If appropriate, enter the type of report, e.g., interim, progress, summary, annual, or final. Give the inclusive dates when a specific reporting period is covered.

5. AUTHOR(S): Enter the name(s) of author(s) as shown on or in the report. Enter last name, first name, middle initial. If military, show rank and branch of service. The name of the principal author is an absolute minimum requirement.

6. REPORT DATE: Enter the date of the report as day, month, year, or month, year. If more than one date appears on the report, use date of publication.

7a. TOTAL NUMBER OF PAGES: The total page count should follow normal pagination procedures, i.e., enter the number of pages containing information.

7b. NUMBER OF REFERENCES: Enter the total number of references cited in the report.

8a. CONTRACT OR GRANT NUMBER: If appropriate, enter the applicable number of the contract or grant under which the report was written.

8b, 8c, & 8d. PROJECT NUMBER: Enter the appropriate military department identification, such as project number, subproject number, system numbers, task number, etc.

9a. ORIGINATOR'S REPORT NUMBER(S): Enter the official report number by which the document will be identified and controlled by the originating activity. This number must be unique to this report.

9b. OTHER REPORT NUMBER(S): If the report has been assigned any other report numbers (*either by the originator or by the sponsor*), also enter this number(s).

10. AVAILABILITY/LIMITATION NOTICES: Enter any limitations on further dissemination of the report, other than those

imposed by security classification, using standard statements such as:

- (1) "Qualified requesters may obtain copies of this report from DDC."
- (2) "Foreign announcement and dissemination of this report by DDC is not authorized."
- (3) "U. S. Government agencies may obtain copies of this report directly from DDC. Other qualified DDC users shall request through _____."
- (4) "U. S. military agencies may obtain copies of this report directly from DDC. Other qualified users shall request through _____."
- (5) "All distribution of this report is controlled. Qualified DDC users shall request through _____."

If the report has been furnished to the Office of Technical Services, Department of Commerce, for sale to the public, indicate this fact and enter the price, if known.

11. SUPPLEMENTARY NOTES: Use for additional explanatory notes.

12. SPONSORING MILITARY ACTIVITY: Enter the name of the departmental project office or laboratory sponsoring (paying for) the research and development. Include address.

13. ABSTRACT: Enter an abstract giving a brief and factual summary of the document indicative of the report, even though it may also appear elsewhere in the body of the technical report. If additional space is required, a continuation sheet shall be attached.

It is highly desirable that the abstract of classified reports be unclassified. Each paragraph of the abstract shall end with an indication of the military security classification of the information in the paragraph, represented as (TS), (S), (C), or (U).

There is no limitation on the length of the abstract. However, the suggested length is from 150 to 225 words.

14. KEY WORDS: Key words are technically meaningful terms or short phrases that characterize a report and may be used as index entries for cataloging the report. Key words must be selected so that no security classification is required. Identifiers, such as equipment model designation, trade name, military project code name, geographic location, may be used as key words but will be followed by an indication of technical context. The assignment of links, rules, and weights is optional.

THE SCATTERING FROM ROUGH CURVED SURFACES OF A WAVE
PROPAGATED THROUGH A RANDOM MEDIUM*

By

Darryl P. Greenwood and E. J. Powers
Department of Electrical Engineering

Technical Report No. 104
June 1, 1971

PLASMA AND QUANTUM ELECTRONICS RESEARCH LABORATORY

ELECTRONICS RESEARCH CENTER
THE UNIVERSITY OF TEXAS AT AUSTIN
Austin, Texas 78712

*Research sponsored in part by the Joint Services Electronics Program
under Research Contract F44620-71-C-0091.

[REDACTED] approved for public release [REDACTED]
distribution is unlimited.

ABSTRACT

A generalized investigation of wave scattering from rough surfaces yields an expression for mean scattered power flux which is the spatial Fourier transform of the product of three transfer functions: (a) the optical transfer function (OTF) of the propagating medium, (b) the joint characteristic function of the surface roughness, and (c) a coherence involving the mean surface and the wave profile. The results are applicable to rough surfaces which have rms slopes less than a few degrees.

The solution is applied to laser scattering from aluminum and titanium airplane surfaces where the medium is the clear atmosphere. Proficorder tracing of sample rough surfaces reveals independent "roughness" and "waveness" components normally distributed with Gaussian (isotropic) autocorrelation. The deterministic surface model is a generalized quadratic approximation to the surface mean. The laser profile is the lowest-order circular laser mode. The atmospheric OTF is modeled as Gaussian.

For typical parameters, the result decouples into a specular term (depending on turbulence, wave profile, and the known surface) and a diffuse component (depending on the rough and known surfaces). The deterministic surface may be deformed spherically to account for an incident wave of slight spherical character. (A spherical wave affects only the coherent scatter.) From a measurement of scatter at normal incidence the surface power spectral density and the atmospheric refractive index structure constant may be determined provided the surface is isotropic, homogeneous, and normally distributed.

Rough surface and profile aspects of the theory are verified by near-field measurements of scatter from titanium and aluminum when there is no turbulence present. Surface power spectral densities found empirically from scatter at normal incidence agree with the spectra found from proficorder tracing.

TABLE OF CONTENTS

	Page
ABSTRACT	ii
LIST OF FIGURES	v
CHAPTER	
I. INTRODUCTION	1
II. GENERALIZED THEORETICAL SCATTERING ANALYSIS	4
A. DETERMINISTIC SCATTERING	4
B. ENSEMBLE AVERAGING	12
III. MODELING OF TRANSFER FUNCTIONS	15
A. ROUGH SURFACE TRANSFER FUNCTION	15
1. Probability Density	16
2. Power Spectral Density	17
3. Form of the RTSF	24
4. Checking Boundary Conditions	25
B. OPTICAL TRANSFER FUNCTION	27
C. DETERMINISTIC TRANSFER FUNCTION	32
D. FINAL INTEGRATED RESULT	34
E. NUMERICAL RESULTS	35
F. SPECIAL CASES	39
1. Incident Spherical Waves	39
2. Normalized Power, Compared with Beckmann	40
3. Direct Backscatter	41
4. Scatter From a Perfectly Smooth Surface	42

LIST OF FIGURES

Fig. No.		Page
1	Surface geometry	5
2	Rotation from a vertical incident polarization to an arbitrary one	11
3	System transfer function model	14
4	Surface height cumulative probability distribution for titanium found from surface tracing	18
5	Surface height cumulative probability distribution for aluminum found from surface tracing	18
6	Individual titanium surface height power spectral density	20
7	Individual aluminum surface height power spectral density	21
8	Average titanium p.s.d.f. and best Gaussian fits to waviness and roughness components	22
9	Average aluminum p.s.d.f. and best fits	23
10	Summation limit m_1 versus argument z for determining the number of terms needed to represent the diffuse component of scatter when $g_1 \approx 1$	26
11	Polar plots of mean scattered power for titanium	38
12	Polar plots of mean scattered power for aluminum	38
13	Polar plots of mean backscattered power	43

	Page
G. THE INVERSE PROBLEM	44
1. Scatter at Normal Incidence	44
2. Direct Backscatter	50
IV. EXPERIMENTAL RESULTS	52
A. EXPERIMENTAL ARRANGEMENT	52
B. MEASUREMENTS	56
1. Preliminary Comments	56
2. Titanium Scatter	57
3. Aluminum Scatter	60
4. Titanium Inverse Measurements	63
5. Aluminum Inverse Measurements	65
6. Conclusions	67
V. CONCLUSIONS	69
APPENDIX	
I. Verification of Inequalities (11) and (18)	71
II. Integration for the Wave Correlation Function	73
III. Relations Between n-dimensional Power Spectra	74
REFERENCES	78

Fig. No.		Page
14	Hypothetical scatter at normal incidence from a slightly rough surface with Gaussian p.s.d.f. and p.d.f. showing relation between e-folding widths and peaks of components	49
15	Hypothetical backscatter (otherwise like figure 14)	49
16a	Experimental set-up for measurement of scattered power	53
16b	Photograph of experimental set-up	54
17	Measured scattered power and theoretical power flux for titanium, $\theta_1 = 27^\circ$	58
18	Measured scattered power and theoretical power flux for titanium, $\theta_1 = 3.5^\circ$	59
19	Measured scattered power and theoretical power flux for aluminum, $\theta_1 = 18^\circ$	61
20	Measured scattered power and theoretical power flux for aluminum, $\theta_1 = 3.5^\circ$	62
21	Titanium two-dimensional power spectral density V_s ...	63
22	Titanium P_s^t (surface height p.s.d.f. from tracing) and P_s^s (surface p.s.d.f. from scattering)	64
23	Aluminum two-dimensional power spectral density V_s ...	65
24	Aluminum P_s^t and P_s^s	66
25	Plot used in determining the approximate Gaussian form for the OTF	74

Chapter I

INTRODUCTION

In the theoretical analysis of electromagnetic wave scattering from rough surfaces, there are three factors in addition to surface roughness which determine the scattering behavior: beam profile, surface curvature, and propagating medium turbulence. The rough surface statistical description is the most important aspect of the problem, and numerous previous investigators (most notably Beckmann [1]) have dwelt mainly on the scattering from zero-mean rough surfaces under spatially uniform illumination. However, when target dimensions are greater than the beam size, the spatial wave profile affects the scattering. Eckart [2] included a beam profile term, but he restricted himself to slightly rough surfaces by approximating the local normal on the surface with the normal direction of the mean plane. Also, surfaces most likely have a mean structure that is not a flat plane. Hence the general surface model is a composite sum of a deterministic and a random component. Except when the beam is propagated through vacuum, the medium will distort the plane character of the wave. Propagation in a turbulent medium is carefully examined by Tatarski [3] and Strohbehn [4] but not in a connotation of surface scattering. We assume the incident wave is plane, but the field profile multiplier is a product of a deterministic term (the profile without turbulence) and a random component (which characterizes the medium).

The expression for scattered power flux is derived from the Helmholtz wave equation and is averaged over ensembles of rough surfaces and incident waves. The final result is a spatial Fourier transform of the product of three coherences (or transfer function). The first transfer function involves the known aspects of the problem -- the wave profile sans turbulence and the known surface component -- and is called the DTF (deterministic transfer function). The second, the familiar optical (or modulation) transfer function (OTF), relates the statistical properties of the medium. Finally, the rough surface transfer function (RSTF) is found from the joint characteristic function of the surface

roughness. The advantage of the transfer function formulation is that some aspects of the problem may be changed without affecting the others.

The expression for mean scattered power is applied to the scattering of laser radiation from rough metallic surfaces where the medium is the clear atmosphere (particle scattering neglected). This application serves as an exemplary use of the generalized result, but more important the problem is the basic research in the study of images generated by scanning a laser beam over a target. In practice a highly-collimated CO_2 or Nd-YAG beam is scanned across the target (in the pattern of a Lissajou or a sinusoid, for example). If the beam size is much less than typical target dimensions, an image may be created by proportionally displaying the received scattered radiation as intensity on a display device such as a CRT. An example of the use of such a system is the identification or classification of aircraft by an air traffic controller. To study the imagery theoretically, we must calculate the power scattered by the surface under the beam at selected points in time. To form a suitable image, we expect surface roughness to give a detectable backscatter level even when the backscatter direction to the detector is not near specular.

The theoretical analysis was carried out because of the inadequacies of previous theories in predicting the propagation and scatter of a laser beam. Medium turbulence (for example atmospheric) becomes most significant when the wavelength is short. Also beam profile and surface curvature are significant when the beam is well-collimated. Certainly profile is unimportant when a microwave radar beam is scattered from an aircraft but becomes significant when the scattering is from the ocean surface. Our results apply at longer wavelengths such as microwave, UHF, or acoustic, but some of the four aspects may be negligible.

In the modeling of the three system transfer functions, the laser beam profile is the lowest order (TEM_{00}) circular mode, the deterministic surface is quadric, and the log-amplitude and phase fluctuations of the wave due to turbulence have isotropic Gaussian statistics. The aluminum and titanium

rough surfaces studied are shown by measurement (tracing on a proficorder to determine instantaneous surface height) and by argument (using the central limit theorem) to be normally distributed. From the measurement, the power spectral density is modeled as a sum of two Gaussians. These two rough surface components are shown to be the "roughness" and "waviness" components of the randomly rough surface.

To justify the use of the models and to verify, in part, the theory, we present measurements of power scattered from aluminum and titanium air-plane surfaces. Since the scattering is from surfaces with a flat mean under laboratory conditions of no turbulence, the measurements are a verification of the rough surface and profile aspects of the theory and model. As a by-product of the theory, we learn how to find the surface statistics from a measurement of scattered power at normal incidence from an isotropic, homogeneous normally-distributed surface. Such measurements are made, and the surface height power spectral densities found are compared with those found in proficorder tracing.

The following sections include: a general derivation for the scattered power, assuming the incident wave and surface are known exactly (ch. II, sect. A); averaging over ensembles of rough surfaces and turbulent waves (ch. II, sect. B); a suitable modeling of the transfer functions which comprise the mean scattered power solution (ch. III, sect. A-E); investigation of special cases (ch. III, sect. F-G); and presentation of experimental results and analysis (ch. IV). Three related mathematical analyses are reserved for the appendix.

Chapter II

GENERALIZED THEORETICAL SCATTERING ANALYSIS

This chapter presents the derivation of the generalized scattering equation which includes the effects of arbitrary wave profile, deterministic surface, rough surface, and the propagating medium. The result allows the user to specify his own surface and wave properties for his particular scattering problem. Chapter III will demonstrate a suitable modeling for the laser scattering problem mentioned in the introduction, but for the present all assumptions are made with the widest range of application.

A. DETERMINISTIC SCATTERING

This section is the derivation of the scattered power where the surface and incident wave are known exactly. The result will be shown to be formally independent of incident polarization. However, initially the scattered electric field for an incident field of horizontal polarization is derived. "Horizontal polarization" implies the incident E-vector is normal to the xz plane of incidence, and the incident H-vector lies in the plane of incidence. (For that plane and for ease in understanding the subsequent definitions, refer to figure 1.) In this section, Beckmann's [1] notation is followed when possible.

The starting point of the derivation is the scalar Helmholtz integral relation for the scattered E-field (E_2) at a receiver point P:

$$E_2(P) = \frac{1}{4\pi} \iint_S \left(E_2 \frac{\partial \psi}{\partial n} - \psi \frac{\partial E_2}{\partial n} \right) ds \quad (1)$$

where in the integrand E_2 and $\frac{\partial E_2}{\partial n}$ are the scattered electric field and its normal derivative on the scattering surface S, and ψ and $\frac{\partial \psi}{\partial n}$ are the Green's function and its normal derivative. Beckmann has the total field at the surface ($E_1 + E_2$, where E_1 is the incident field) in the integral rather than just the scattered field. However, Stakgold [5] shows the two expressions are equal by proving

$$\iint_S \left(E_1 \frac{\partial \psi}{\partial n} - \psi \frac{\partial E_1}{\partial n} \right) ds \equiv 0. \quad (2)$$

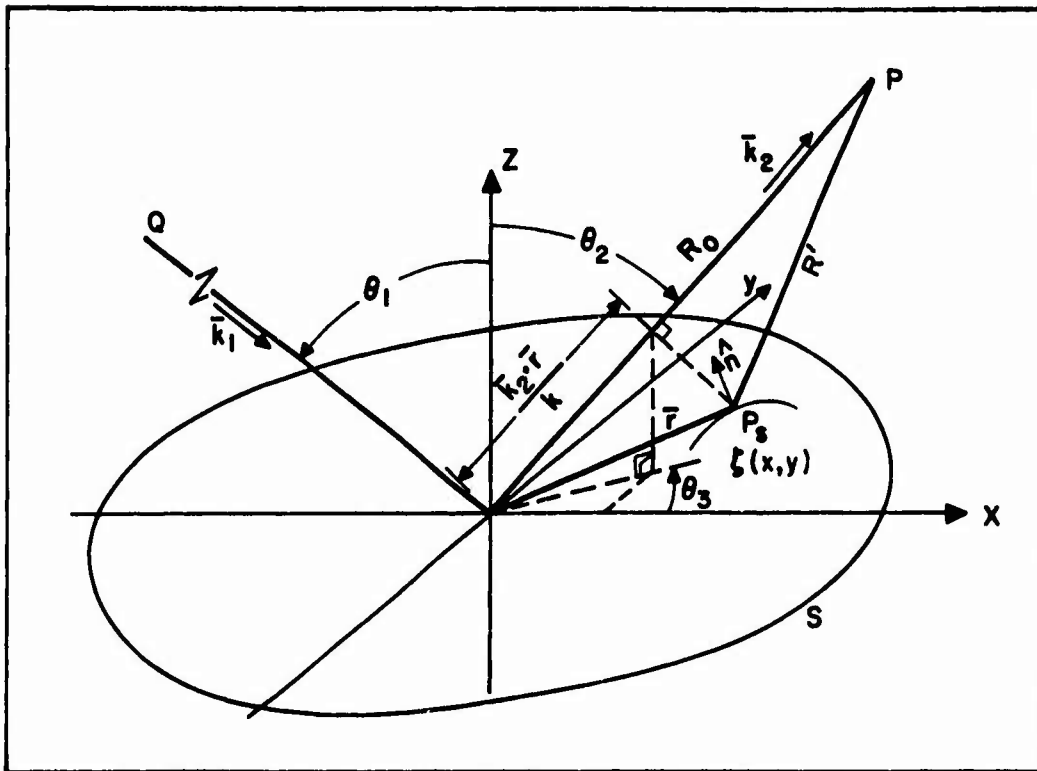


Figure 1. Surface geometry. (Only one surface point, P_s , is depicted to reduce complexity.)

The appropriate Green's function is

$$\psi = \frac{\exp(ikR')}{R'} \quad (3)$$

where k is the wave number and R' is the variable distance from P to a surface point P_s . If the receiver point P is in the far-field, only the first two terms of the power series for R' need be kept:

$$kR' \approx kR_0 - \bar{k}_2 \cdot \bar{r} \quad (4)$$

where R_0 is the (constant) range, \bar{k}_2 is the propagation vector directed from the origin to P , and

$$\bar{r} = \bar{x} + \bar{y} + \zeta(x, y) \hat{z}. \quad (5)$$

(The hat (^) above the letter indicates a unit vector: for example $\hat{z} = \bar{z} / |\bar{z}|$.)

The familiar ζ is chosen as the surface height function. From (3) and (4) we find

$$\frac{\partial \psi}{\partial n} \approx -i \bar{k}_2 \cdot \hat{n} \psi \quad (6)$$

and

$$\psi \approx \frac{\exp(ikR_0)}{R_0} \exp(-i \bar{k}_2 \cdot \bar{r}). \quad (7)$$

In the far-field limit, the vector directed from P_s to P is assumed to have the unit vector \bar{k}_2/k .

The incident electric field is assumed harmonic and nearly plane:

$$E_1(\bar{r}, t) = U(\bar{r}) \exp(i \bar{k}_1 \cdot \bar{r} - i \omega t). \quad (8)$$

(In keeping with Beckmann notation, sub-1 implies an incident quantity; sub-2, scattered. As usual, the temporal frequency is ω , and t is time.) The wave profile factor $U(\bar{r})$ is complex in general and includes (a) the deviation of the E-field from a pure plane wave (due to scintillation), and (b) the original spatial profile at the wave source. In equation (8), \bar{k}_1 is a propagation vector directed from the far-field source point Q to the origin of the scattering system.

The tangent plane approximation is made as a preliminary to a Kirchhoff boundary condition. The surface must have large local radii of curvature with respect to λ , the wavelength, for the approximation to be reasonable. Moreover, the slope along the surface must be small (less than a few degrees) so that the incident polarization on the plane as a whole is equivalent to the polarization on the individual tangent planes. Both Leader [6] and Valenzuela [7] have shown that depolarization is an effect of multiple scattering; but since small slope and large radius of curvature are assumed here, the surface roughness is slight to moderate, and multiple scattering will be insignificant. Finally, since the simple plane-wave reflection problem is solved to establish the boundary conditions on a single tangent plane, we are justified in using the Fresnel horizontal reflection coefficient R^- in expressing the scattered E-field at the surface as R^- times the incident field there:

$$E_2 \Big|_S = R^- E_1 \Big|_S . \quad (9)$$

What to use for the Fresnel coefficient is a subject of continuing argument; however, for present purposes, we assume R^- is not a function of the integration variables of (1). This is at least valid for infinitely conductive surfaces; and as an approximation for other surfaces, an average R^- taken over the surface for a given incident angle might be sufficient. Error for this type of average increases with increasing roughness of the surface, but once again the tangent-plane approximation restricts us to moderately rough surfaces.

The normal derivative boundary condition is also found from the tangent-plane reflection problem:

$$\frac{\partial E_2}{\partial n} \Big|_S = E_1 R^- (-i\bar{k}_1 \cdot \hat{n} + \frac{1}{U} \frac{\partial U}{\partial n}) \Big|_S \quad (10)$$

In most circumstances the second term in the parentheses in (10) is negligible. Mathematically we require

$$\left| \frac{1}{k U \cos \theta_1} \frac{\partial U}{\partial z} \right| \ll 1 , \quad (11)$$

and that the surface slopes (ζ_x, ζ_y) be much less than unity. This says grazing incidence is avoided, and the gradient of U normal to the mean surface is smaller than kU . There is an example of a verification of (11) in appendix I wherein the inequality is checked for the models presented in chapter III. Satisfying (11) also implies there is only a slight variation in U in the z -direction over distances the order of the wavelength and hence of the composite surface. If the Maclaurin series in z for $U(\bar{r})$ is written:

$$U(\bar{r}) = U(x, y, 0) + \frac{\partial U}{\partial z} \Big|_{z=0} z + \dots , \quad (11a)$$

then by inequality (11) only the first term in the series need be kept:

$$U(\bar{r}) \approx U(x, y). \quad (12)$$

After putting (6), (7), (8), (9), (10), and (12) into (1), dropping the time-harmonic factor, and performing vector-algebra manipulation:

$$E_2(P) = \frac{R^{-1} \exp(ikR_0)}{4\pi R_0} \iint_{-\infty}^{\infty} U e^{i\bar{v} \cdot \bar{r}} [-\zeta_x v_x - \zeta_y v_y + v_z] dx dy \quad (13)$$

$$\text{where } \bar{v} = \bar{k}_1 - \bar{k}_2 = v_x \hat{x} + v_y \hat{y} + v_z \hat{z} \quad (14)$$

$$= k [(\sin \theta_1 - \sin \theta_2 \cos \theta_3) \hat{x} - \sin \theta_2 \sin \theta_3 \hat{y} - (\cos \theta_1 + \cos \theta_2) \hat{z}].$$

(Subscripts x and y, when appearing on ζ or U , imply those partial derivatives.)

Equation (13) is the first reasonable form for use when U and ζ are exactly known, but without further approximation the integral is revised via partial integration such that the derivatives appear on U rather than ζ :

$$E_2(P) = C_1 R^{-1} \iint_{-\infty}^{\infty} [U - \frac{i}{v^2} (v_x U_x + v_y U_y)] e^{i\bar{v} \cdot \bar{r}} dx dy \quad (15)$$

$$\text{where } C_1 = \frac{ik \exp(ikR_0)}{2\pi R_0} (\cos \theta_1 - \frac{v_x}{v_z} \sin \theta_1) \quad (16)$$

$$\text{and } v^2 = \bar{v} \cdot \bar{v} = 2k^2 (1 - \sin \theta_1 \sin \theta_2 \cos \theta_3 + \cos \theta_1 \cos \theta_2). \quad (17)$$

Reduction of (15) by eliminating the second term in the bracket requires (for each (x, y) and $(\theta_1, \theta_2, \theta_3)$):

$$\frac{|U| v^2}{2k (|U_x| + |U_y|)} \gg 1. \quad (18)$$

Loosely, (18) is satisfied if (a) there are no edges or sharp boundaries (shadowing is neglected); (b) k is large (this is consistent with the local radius of curvature being much larger than λ); and (c) if $\theta_3=0$, then $\theta_1 = \theta_2 \neq \pm \pi/2$ (grazing incidence is avoided if the observer at P "looks at" the specularly scattered component). If (18) is indeed satisfied, then the expression for scattered E-field of horizontal polarization for known U and ζ is

$$E_2(\bar{v}) = C_1 R^{-1} \iint_{-\infty}^{\infty} U e^{i v_z \zeta} e^{i(v_x x + v_y y)} dx dy \quad (19)$$

which is written to emphasize the Fourier kernel. Like inequality (11), the validity of inequality (18) is checked in appendix I for the specific field profile and medium turbulence model of chapter III.

The above result is also applicable to scattering of a vertically polarized incident electric field:

$$\begin{aligned}\bar{E}_1 &= U(\bar{r}) [\hat{x} \cos \theta_1 + \hat{z} \sin \theta_1] \exp(i\bar{k}_1 \cdot \bar{r} - i\omega t) \\ &= E_{1x} \hat{x} + E_{1z} \hat{z}\end{aligned}\quad (20)$$

or an H-field of either polarization. The new electric field boundary conditions are

$$\bar{E}_2 \Big|_S = R^+ (-E_{1x} \hat{x} + E_{1z} \hat{z}) \Big|_S \quad (21)$$

$$\text{and} \quad \frac{\partial E_2}{\partial n} \Big|_S = R^+ (i\bar{k}_1 \cdot \hat{n} - \frac{1}{U} \frac{\partial U}{\partial n}) (E_{1x} \hat{x} - E_{1z} \hat{z}) \Big|_S \quad (22)$$

where R^+ is the vertical Fresnel coefficient. (For the forms for R^+ and R^- , see Beckmann [1], p. 21.) Because of the similarities between (9) and (21), and (10) and (22), the steps leading to the scattering equation (19) are found to be applicable to each of the two scalar components of the scattered field (termed E_{2x} and E_{2z}) where the incident field is vertically polarized. The (scalar) Euclidean norm ($\sqrt{E_{2x}^2 + E_{2z}^2}$) of the scattered field is the desired quantity since it is the field observed by a receiver at P looking along \bar{k}_2 . That scalar scattered field is also given by (19) if we employ inequality (11) again and let $R^- \rightarrow R^+$. The scattered magnetic fields are then found by duality. For example, to derive the scattered H-field due to an incident H lying normal to the incident plane, replace the E in the derivation of scattered E-field for horizontal polarization by H, and let $R^- \rightarrow R^+$.

The real scattered power (flux) is now easily written for either vertical or horizontal polarization:

$$\begin{aligned}P_2 &= \frac{1}{2} E_2 H_2^* \\ &= \frac{Y_0}{2} |C_1|^2 R^2 \int_{-\infty}^{\infty} \int_{-\infty}^{\infty} G_d(v_z; \bar{\Delta}) e^{i\bar{v} \cdot \bar{\Delta}} d\bar{\Delta}\end{aligned}\quad (23)$$

where R is the reflection coefficient of the appropriate polarization, and Y_0 is the admittance of free space. The function G_d in (23) is an unnormalized

mutual coherence:

$$\begin{aligned} G_d(v_z; \bar{\Delta}) &= \langle V_1^* V_2 \rangle \\ &= \int_{-\infty}^{\infty} \int_{-\infty}^{\infty} V^*(x, y) V(x+\Delta x, y+\Delta y) dx dy \end{aligned} \quad (24)$$

where $V = U \exp(iv_z \zeta)$ is known exactly. (The sub-d is for "deterministic.")

Moreover, for simplicity:

$$\bar{v}_1 = v_x \hat{x} + v_y \hat{y}$$

is a spatial frequency,

$$\bar{\Delta} = \Delta x \hat{x} + \Delta y \hat{y}$$

is a spatial distance, and

$$d\bar{\Delta} = d\Delta x \ d\Delta y. \quad (25)$$

In a coherence in the "bra-ket" form in (24), the convention is to take (x, y) as the subscript 1, and $(x + \Delta x, y + \Delta y)$ as sub-2. Not only is the functional form of G_d a coherence, but the Fourier transform in (23) of G_d is a power spectral density function. Furthermore, note that in general a covariance $B(\bar{\Delta})$ which is defined by

$$B(\bar{\Delta}) = \langle (V_1 - \langle V_1 \rangle)^* (V_2 - \langle V_2 \rangle) \rangle \quad (25a)$$

is in turn related to the coherence by rewriting (25a):

$$B(\bar{\Delta}) = \langle V_1^* V_2 \rangle - \langle V_1^* \rangle \langle V_2 \rangle, \quad (25b)$$

and that a correlation $C(\bar{\Delta})$ is defined by

$$C(\bar{\Delta}) = \frac{B(\bar{\Delta})}{B(\bar{0})}. \quad (25c)$$

In general, the incident polarization is neither purely vertical nor horizontal but is arbitrary. When superposition is used on the incident E and H fields to represent an arbitrary polarization, one finds that the relation (23) is still applicable. Suppose E_1 is rotated through an angle α from the incident plane about the propagation vector \bar{k}_1 (as depicted in figure 2). Then the coefficient R^2 needs only to be redefined:

$$R^2 = (R^+ \cos \alpha)^2 + (R^- \sin \alpha)^2. \quad (26)$$

However, the integrals (23) and (24) are unaltered. The preceding polarization analysis indeed shows that the term "scalar scattering" is still appropriate even when the incident fields are of arbitrary polarization. In fact the question of incident polarization can be ignored since it is obviously a matter of choosing the proper form for R^2 . From now on, the case of a perfect reflector ($R^2 = 1$) is taken without significant loss of generality.

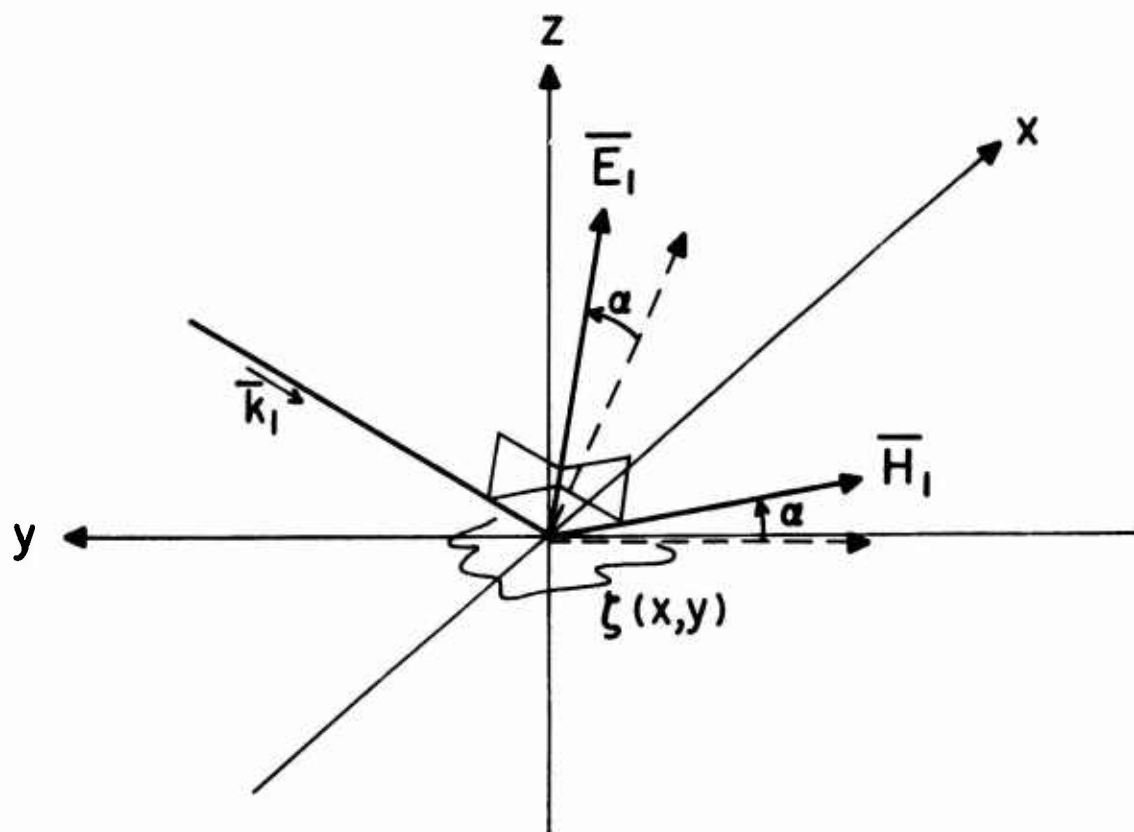


Figure 2. Rotation from a vertical incident polarization (dashed lines) to an arbitrary one. Note each vector \bar{E}_1 and \bar{H}_1 can now be split into vertically and horizontally polarized components.

B. ENSEMBLE AVERAGING

Since very often in scattering the surface is not exactly known, the scattered power as averaged over an ensemble of random surfaces is needed. The actual surface model chosen is a sum of a randomly rough (ζ_r) and a deterministic surface (ζ_d):

$$\zeta = \zeta_r + \zeta_d. \quad (27)$$

The rough surface is described by its second order statistics and is assumed to be statistically homogeneous (stationary) on the area under the beam. The joint probability density of the random variable ζ_r is $W(z_1, z_2; \Delta x, \Delta y)$, and the joint characteristic function is the double Fourier transform:

$$\begin{aligned} \chi(v_1, v_2; \bar{\Delta}) &= \iint_{-\infty}^{\infty} W(z_1, z_2; \bar{\Delta}) e^{i(v_1 z_1 + v_2 z_2)} dz_1 dz_2 \\ &= \langle e^{i(v_1 z_1 + v_2 z_2)} \rangle. \end{aligned} \quad (28)$$

(The reader should be careful not to confuse the statistical characteristic function (28) with the deterministic coherence function (24) even though the bracket notation is the same.) The surface ensemble average is now taken on P_2 given by (23):

$$\langle P_2 \rangle = \frac{Y_0}{2} |C_1|^2 \iint_{-\infty}^{\infty} G_d(v_z; \bar{\Delta}) \chi(v_z; \bar{\Delta}) e^{i\bar{v}_\perp \cdot \bar{\Delta}} d\bar{\Delta} \quad (29)$$

where G_d is as in (24) except now $\zeta \rightarrow \zeta_d$, and

$$\chi(v_z; \bar{\Delta}) = \chi(v_z, -v_z; \bar{\Delta}). \quad (30)$$

Homogeneity of ζ_r allowed the χ to be extracted from the integral defining G_d . If the surface model chosen were a more general higher order composite:

$$\zeta = \zeta_d + \sum_{i=1}^{n_s} \zeta_{r_i} \quad (31)$$

and if χ_i is the joint characteristic function of ζ_{r_i} , then in (29):

$$\chi(v_z; \bar{\Delta}) = \prod_{i=1}^{n_s} \chi_i(v_z; \bar{\Delta}) \quad (32)$$

if $\{\zeta_{r_1}\}$ is a mutually independent set.

Next, rather than assuming exact knowledge of the incoming wave, an average over an ensemble of incoming waves U is taken. The field profile is rewritten as the product:

$$U = \mathcal{E} Z \quad (33)$$

where \mathcal{E} is the deterministic character of the incident field, and Z is a homogeneous random variable whose statistics are assumed known. The random variable Z is the output of a turbulent medium where the input is a spatially uniform illumination of unity amplitude. (Hence Z is itself unitless.) A second averaging is then performed on the mean scattered power over the ensemble of incident waves:

$$\langle \langle P_2 \rangle \rangle = \frac{Y_0}{2} |C_1|^2 \int_{-\infty}^{\infty} \int_{-\infty}^{\infty} G_d(v_z; \bar{\Delta}) \chi(v_z; \bar{\Delta}) C_0(\bar{\Delta}) e^{i\bar{v}_1 \cdot \bar{\Delta}} d\bar{\Delta} \quad (34)$$

where $C_0(\bar{\Delta}) = \langle Z_1^* Z_2 \rangle$ is a statistical mutual coherence (unnormalized), and the G_d is still defined by (24) except now $U \rightarrow \mathcal{E}$ and $\zeta \rightarrow \zeta_d$. In obtaining (34), the homogeneous property of the medium (and hence of Z) is used to extract C_0 from the integral defining G_d . The model for the wave profile (33) is especially chosen to yield this decoupling, since U itself is non-homogeneous.

Relation (34) is the most general form for mean scattered power flux to be obtained here. It sets forth the four contributors to the problem -- the incident wave, transmitting medium turbulence, the deterministic surface, and the rough surface. It quite obviously reduces to the earlier, less general scattering equations (23) and (29). This extends Beckmann's result in that his involves only the rough surface. Three special cases are notable: (a) if the rough surface goes to zero, $\chi \rightarrow 1$; (b) if there is no turbulence, $C_0 \rightarrow 1$; and (c) if the mean surface is a flat plane ($\zeta_d = 0$), G_d becomes the mutual coherence which Eckart [2] found as part of his result:

$$\begin{aligned}
 G_d \Big|_{\zeta_d=0} &= \iint_{-\infty}^{\infty} e^*(x, y) e(x + \Delta x, y + \Delta y) dx dy \\
 &= \langle e_1^* e_2 \rangle.
 \end{aligned}
 \tag{35}$$

The above integral may also be termed the incident wave coherence.

Interpretation of (34) is best done via a systems transfer function viewpoint. Since (34) is a Fourier transform (where \bar{v} is spatial frequency), each component of the integrand (except the kernel) can be interpreted as a transfer function, as exemplified by the "system" of figure 3. In usual terminology C_o is the optical (or modulation) transfer function (OTF). Let G_d and χ be defined as the deterministic and rough surface transfer functions (DTF and RSTF), respectively. The "input" to the system is the constant factor $\frac{1}{2} Y_o |C_1|^2$. The amplitude of the incident wave is in the DTF G_d . Because of the decoupled nature of the result, certain aspects of the problem (such as the rough surface) can be revised without varying others (deterministic components and the turbulence).

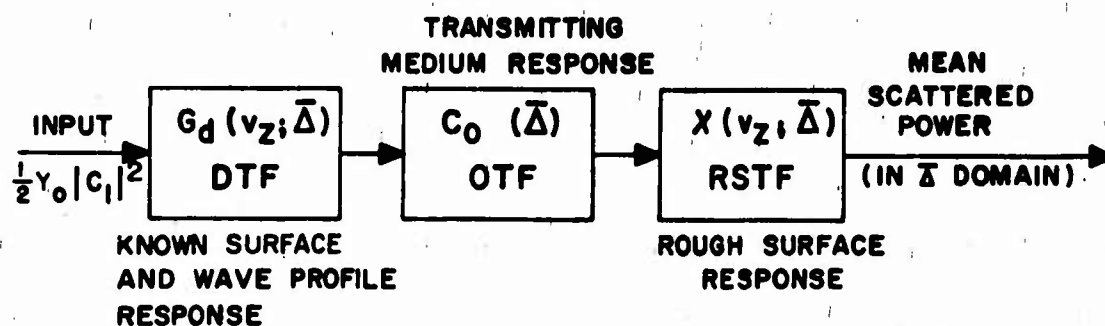


Figure 3. System transfer function model for the mean scattered power as given by equation (34).

Chapter III

MODELING OF TRANSFER FUNCTIONS

The general solution (34) is now applied to the scattering of laser radiation from rough curved surfaces where the propagating medium is the clear atmosphere. This serves as an exemplary use of the result and more important gives the desired theoretical information on scattering from the titanium and aluminum airplane surfaces. Initially the rough surface statistics are investigated to find the RSTF; then the OTF and DTF are found. Although these models are optimal for the problem at hand, they are also applicable in numerous parallel situations. The advantage of the formulation (34) is that inappropriate transfer functions may be remodeled without disturbing the others. For example, suppose after calculating the scatter from the titanium surface in the atmosphere, we desire the scatter from the same surface under water. Then the new OTF would be determined but the remainder of the analysis would remain intact.

A. ROUGH SURFACE TRANSFER FUNCTION

The aluminum studied was taken from a scrapped USAF F-84 tail section. Because the part had been in extensive use, it is more typical of aircraft in use today than an unused sample would be. Aluminum is generally used in sub-Mach 2.5 aircraft, and titanium in Mach 2.5 and up. The titanium studied is a sample used in stress testing. Since titanium does not corrode as aluminum does, it too is typical of present-day aircraft materials. Other samples which were not investigated were (a) a painted one, since presently paint of military aircraft is classified and hence unavailable; (b) composite materials such as Boron/Epoxy and Graphite/Epoxy which are formed by a process which does not obey the central limit theorem. In fact, the composites exhibit a nearly periodic surface. Moreover, neither composite nor painted surfaces have a near-unity reflection coefficient.

To establish the RSTF, the second-order statistics of the rough surface must be found by directly probing the surface. Since the surfaces under study are optically rough, the proper instrument is a proficorder. A proficorder (Bendix trade-name) drags a stylus slowly across a surface and produces an output proportional to surface height. The analog output is recorded and converted to digital form for computer analysis. In our case, the recording was made on a strip-chart and the conversion was manual. Traces were made on the surfaces at various locations to check for homogeneity (stationarity); moreover at some locations, traces at 90° and 45° to each other were made to check for isotropy. A total of six traces with number of points ranging from 128 to 512 were taken for the aluminum to give a total number of 1920 data points for analysis. There were four titanium traces, each with 128 data points. The sample period was 0.2 mil; hence trace lengths ranged from 25.6 to 102.4 mil in length. The first step in computer analysis is the removal of a linear trend and mean to minimize surface orientation errors. The output of the program includes probability density (p.d.f.), cumulative distribution (c.d.f.), and power spectral density (p.s.d.f.).

1. Probability Density.

Williamson [8], [9] has shown that to remarkable accuracy most randomly-prepared metallic surfaces possess a Gaussian probability density. For surfaces where the preparation technique is a cumulative result of a large number of repeated events occurring randomly over the surface, the central limit theorem applies and insures a nearly normal probability density [8]. Such preparation must completely define the surface roughness; it cannot merely reshape maxima. Hence sanding, sand blasting, corrosion, and rolling of sheet metal may generate a normal density; whereas light polishing and buffing may not. Moreover, if the effect of these processes is distributed uniformly over the surfaces, the statistics will be homogeneous. And if the process operates without "preferred direction", the statistics are isotropic. Hence the above-mentioned processes should generate isotropic,

homogeneous normal statistics. (An example of a non-isotropic, but homogeneous random surface is the ocean. Here, the wind direction is the preferred direction.) Rather than relying completely on this heuristic approach, the surfaces are checked for p.d.f., isotropy, and homogeneity.

The probability density of the aluminum and titanium surfaces was obtained by the histogram method suggested by Jenkins and Watts [10]. To see how close to a Gaussian the p.d.f. is, the c.d.f. was found by a cumulative summation of the p.d.f. and was plotted on probability paper. The composite c.d.f. for titanium in figure 4 and for aluminum in figure 5 (indicated by "total") closely follow a straight line; so these surfaces are nearly normally distributed. That straight line is the c.d.f. corresponding to a Gaussian p.d.f. which has the same variance and mean as found for the sample. In figure 4, the abscissa is normalized to the standard deviation; however the abscissa in 5 is not normalized. The two c.d.f.'s in figure 4 labeled "roughness" and "waviness" are explained in part 2 of this section. Not only were the composite p.d.f.'s nearly Gaussian, but the c.d.f. for each surface trace (not shown) closely followed the straight line as well. The individual standard deviations are given in the captions of figures 6 and 7. The properly-weighted average standard deviations are : aluminum 0.067μ ; titanium 0.095μ . From this information we can conclude the assumption of stationarity to first order is reasonable. We still need to show second order homogeneity is valid.

2. Power Spectral Density.

Since the surfaces can be suitably represented by a normal p.d.f., all that remains in completely defining the surface second-order statistics is a measurement of the power spectral density, P_s . The p.s.d.f. is obtained through the following steps: (a) taking the (fast) Fourier discrete series expansion of the data, (b) applying a Hanning window as a three-point convolver, (c) taking the modulus-square of the resultant sequence as a raw estimate of power, and (d) averaging over bands of frequency to improve confidence limits. (The final limits, or error bars, were evaluated from the table

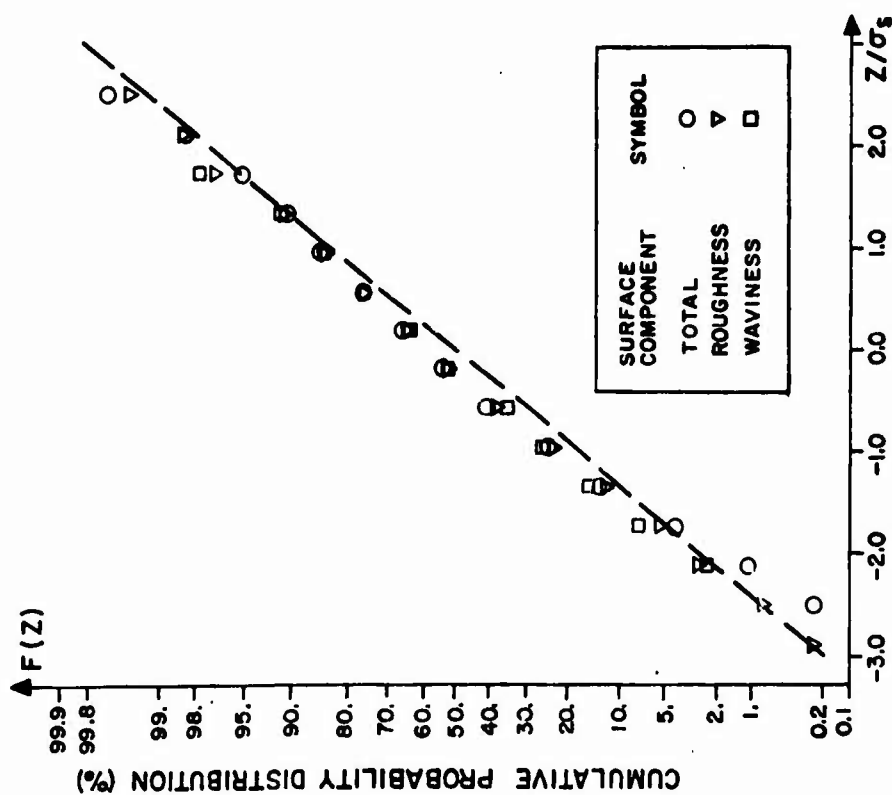


Figure 4. Surface height cumulative probability distribution for titanium found from surface tracing. Distribution for total surface and surface components are versus a normalized abscissa.

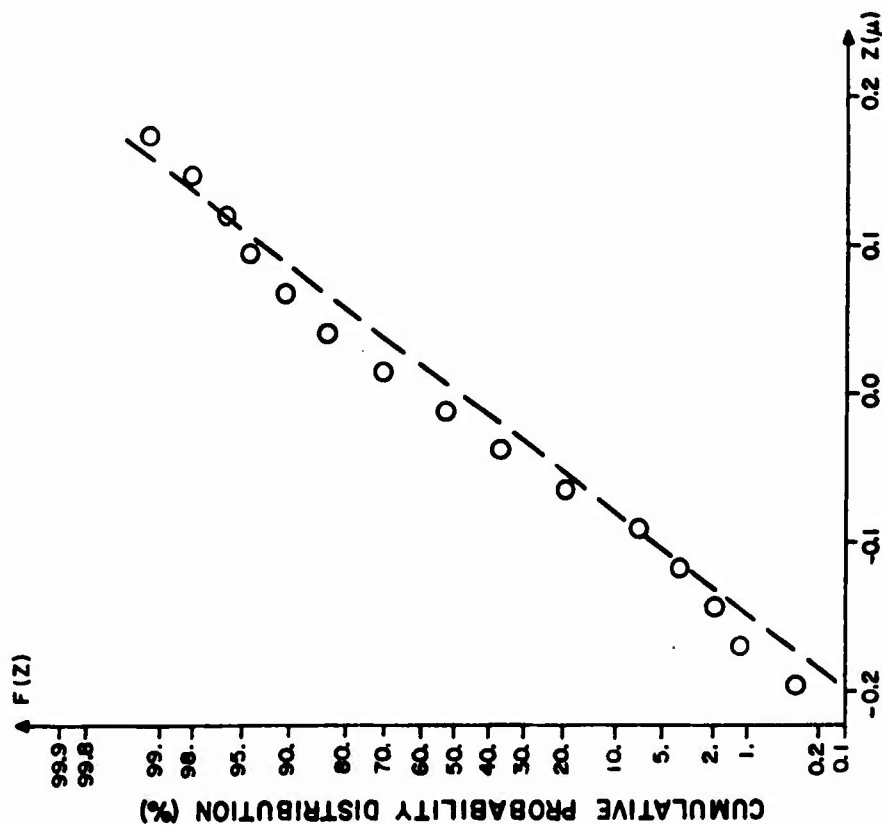


Figure 5. Surface height cumulative probability distribution for aluminum found from surface tracing. Abscissa is not normalized but is the actual surface height.

provided by Blackman and Tukey [11].) The individual p.s.d.f.'s for each of the four titanium traces are shown in figure 6; and figure 7 has the six aluminum p.s.d.f.'s. The titanium spectra display the expected isotropic and homogeneous behavior; however the aluminum is at best only isotropic and locally homogeneous in that traces labeled 1,2,3 are at one location on the surface and traces 4,5,6 are one inch away. The poor behavior of the aluminum is due to non-uniform corrosion of the surface. Hence for the aluminum, an averaged power spectrum is used to represent the entire surface. Since the titanium appears stationary (to second order), averaging of titanium P_g improves confidence limits. (Titanium averaged p.s.d.f. is in figure 8; aluminum, figure 9.) When scattering measurements are made and compared with theoretical curves which use these averaged spectra, we will observe a good match which confirms the necessity of taking the average for aluminum.

We notice that there are two regions in which the power is located. The low frequency power is termed the "waviness" component because of the long wavelengths. Waviness is a result of the rolling process that formed the metal. Similarly, the wide-band component is termed "roughness". The origin of the roughness component is partly the process which formed the metal originally and partly the processes that act on the surface after formation (e.g. corrosion in the case of aluminum). Because of the multiple-application of events to create the random surface structure in surface formation and in the post-formation processes, we expect the roughness and waviness components each to be normally distributed. Each surface trace was then filtered into its two components, and each was investigated for c.d.f. Once again the experimental results confirm the expected Gaussian p.d.f. The c.d.f.'s of the individual titanium components are shown in figure 4 wherein the abscissa of each is normalized to the individual standard deviation.

Since the two surface components appear to be created by independent processes (even in sheet rolling the small-scale fluctuations are not related to large-scale), the components are themselves independent. Hence the sum of the individual power spectra equals the total spectrum, and

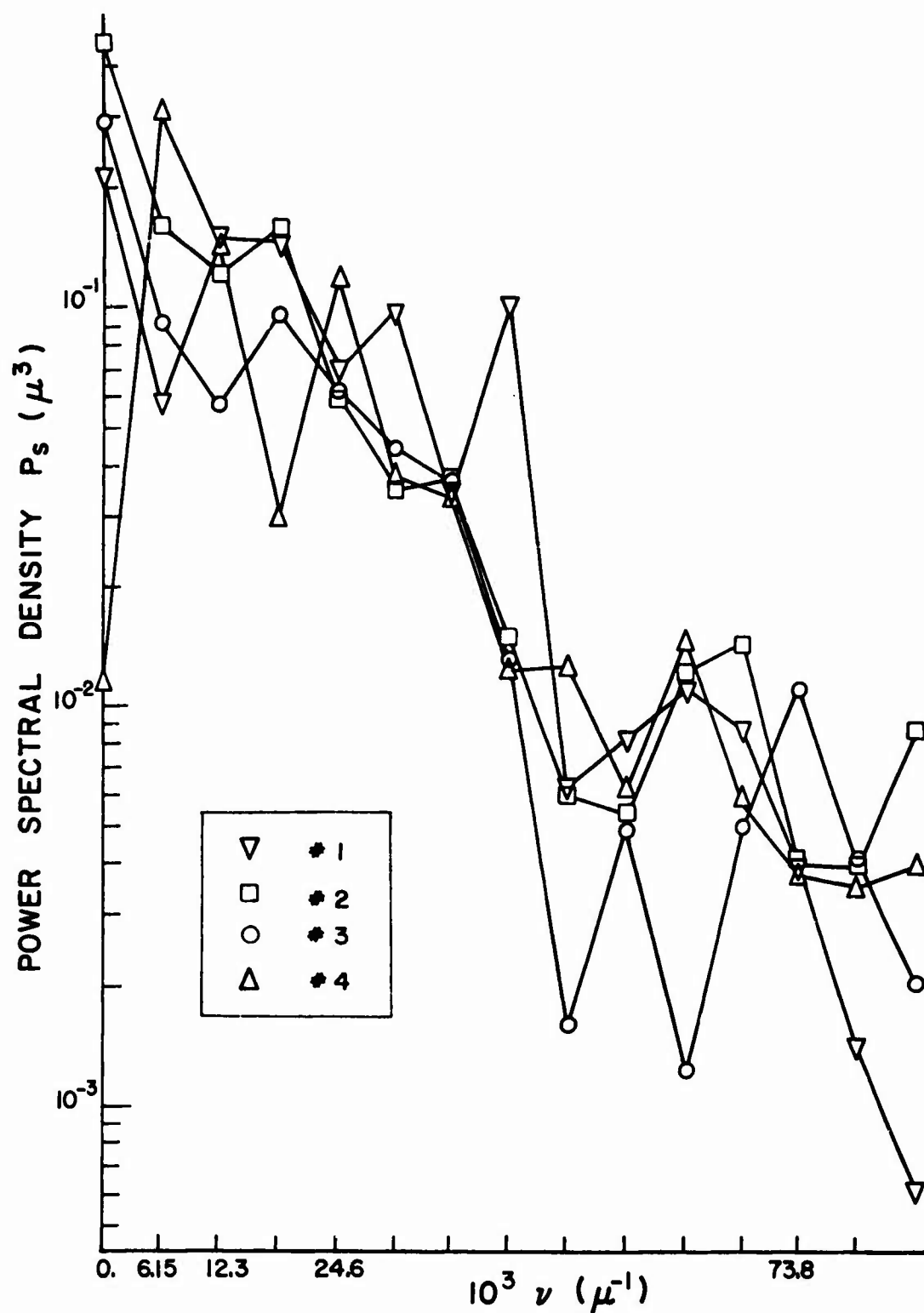


Figure 6. Individual titanium surface height power spectral density versus wavenumber ν . (Each trace has 128 data points. Individual standard deviations (in μ) are 0.099 (#1), 0.102 (#2), 0.084 (#3), and 0.094 (#4). Nyquist frequency is $0.0984 \mu^{-1}$.)

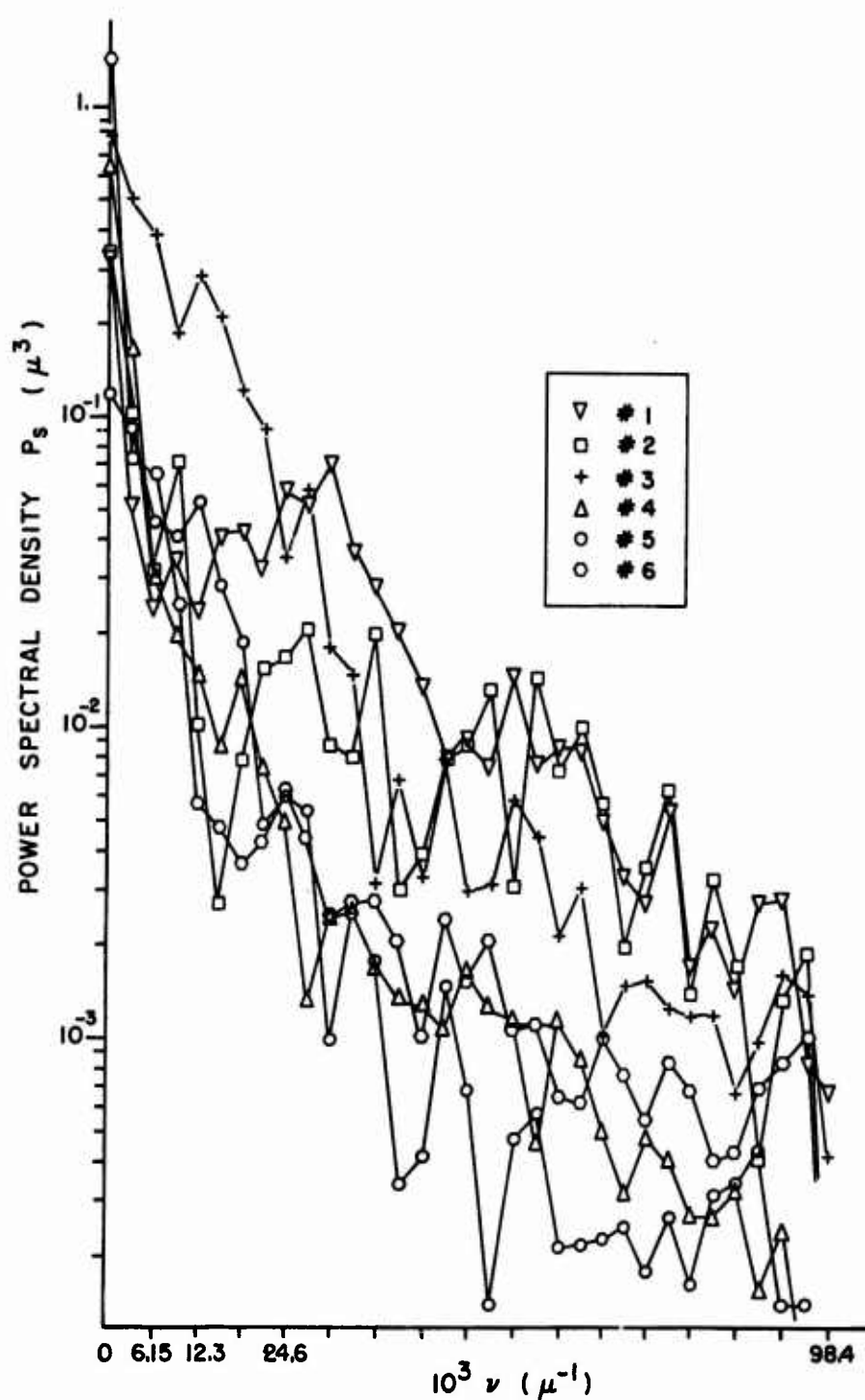


Figure 7. Individual aluminum surface height power spectral density versus wavenumber ν . Confidence limits are not shown due to non-stationarity. (Individual standard deviations (in μ) followed by number of data points are 0.072, 512 (#1); 0.062, 128 (#2); 0.125, 256 (#3); 0.063, 256 (#4); 0.049, 256 (#5); 0.077, 512 (#6). Nyquist frequency is $0.0984 \mu^{-1}$.)

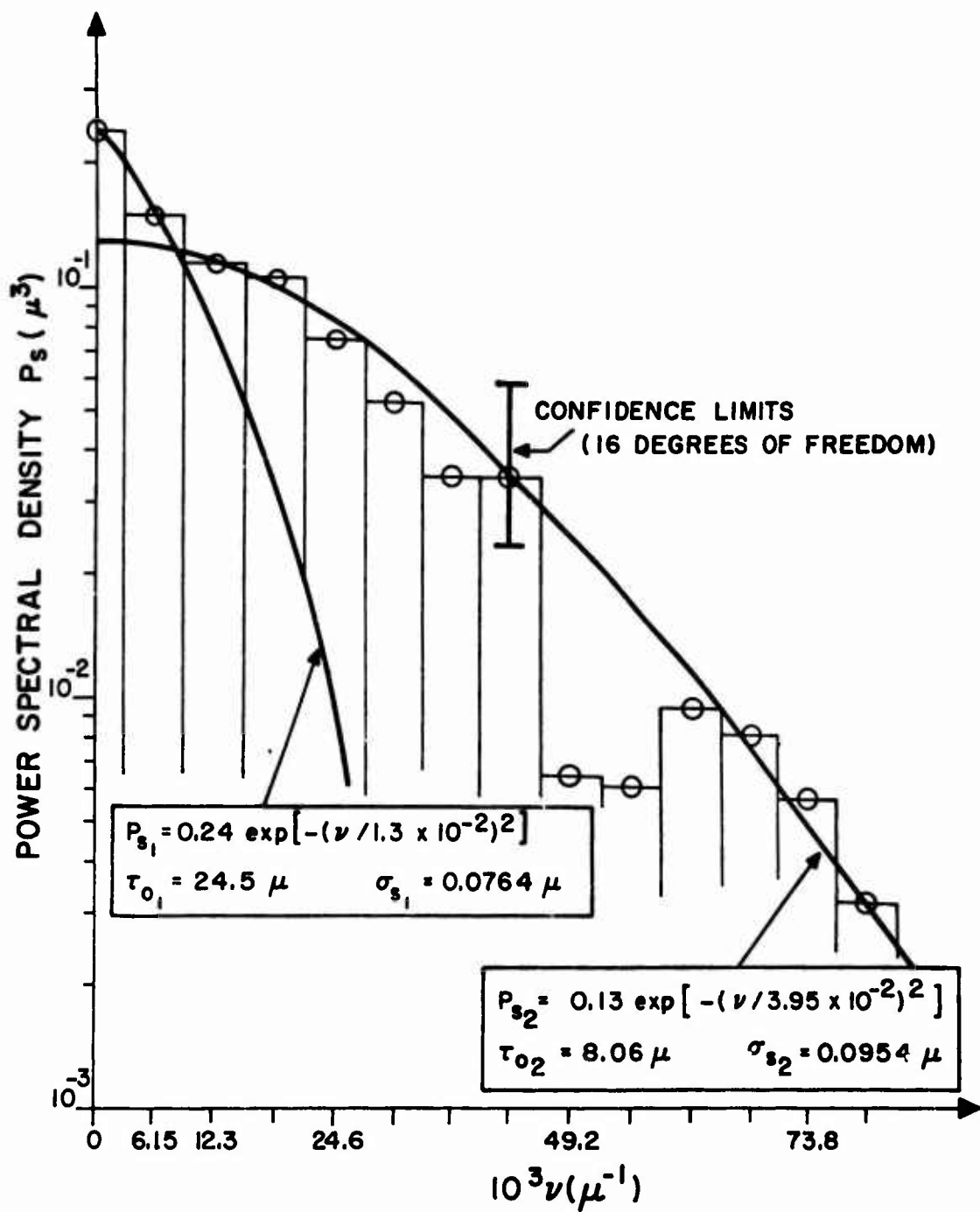


Figure 8. Average titanium p.s.d.f. and best Gaussian fits to waviness (low-frequency) and roughness (high-frequency) components.

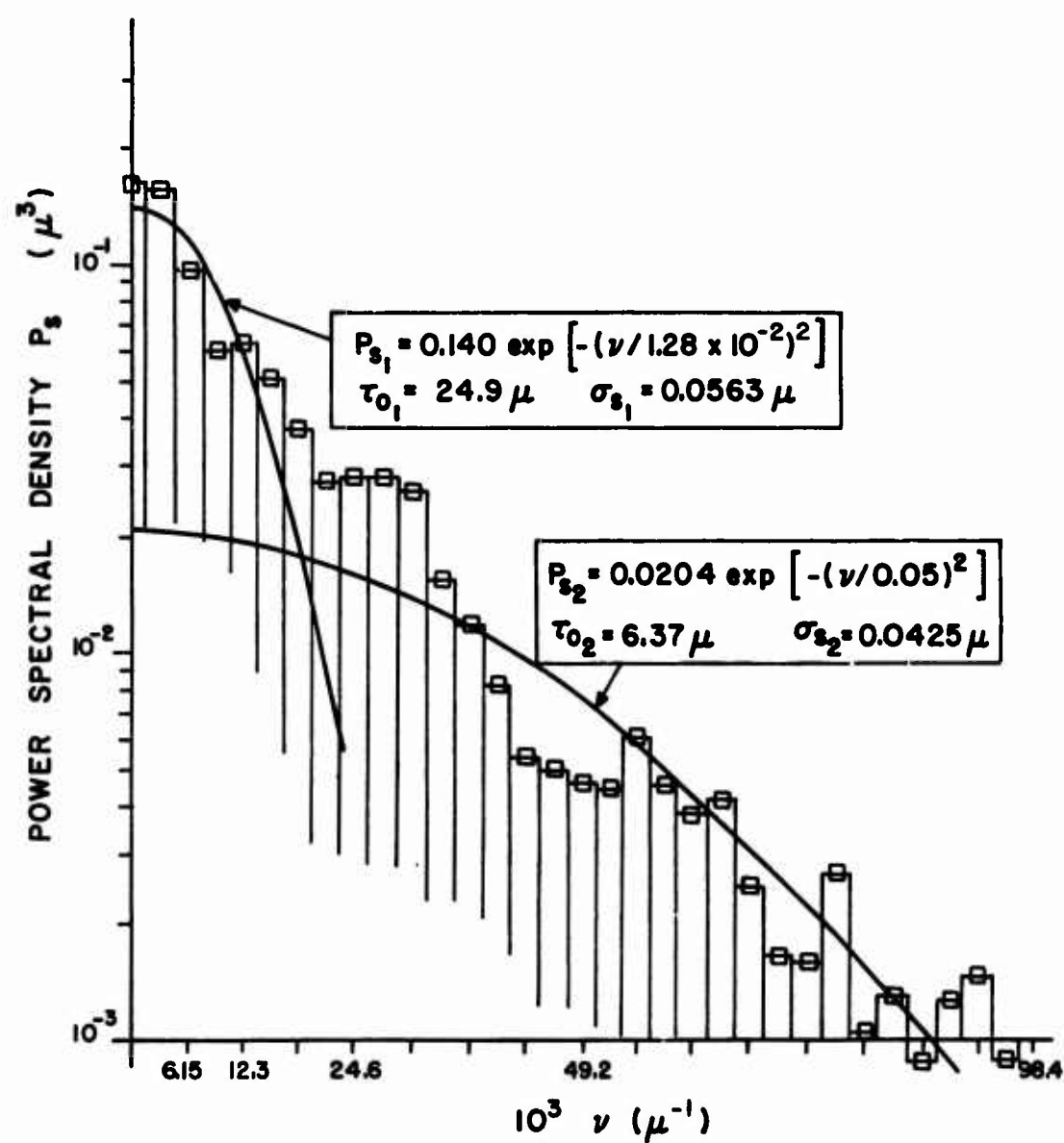


Figure 9. Average aluminum p.s.d.f. and best fits.

the surface characteristic function can be written as the product of individual characteristic functions. For the individual power spectra P_{s_i} , a Gaussian model is closely fitted to the data (see figures 8 and 9):

$$P_{s_i}(v) = P_{s_i}(0) \exp \left[- (v/v_{o_i})^2 \right] \quad (36)$$

where v is spatial frequency and v_{o_i} is the e-folding frequency of the Gaussian. Consequently, the individual surface autocorrelation functions are the Fourier-cosine transforms of $P_{s_i}(v)$:

$$C_{s_i}(\tau) = \int_{-\infty}^{\infty} \cos(2\pi v \tau) P_{s_i}(v) dv. \quad (36a)$$

$$\text{Hence } C_{s_i}(\tau) = \exp \left[- (\tau/\tau_{o_i})^2 \right] \quad (37)$$

$$\text{where } \tau^2 = (\Delta x)^2 + (\Delta y)^2, \quad (38)$$

$\tau_{o_i} = (\pi v_{o_i})^{-1}$, and $\sigma_{s_i}^2 = P_{s_i}(0) v_{o_i} \sqrt{\pi}$ is the individual surface variance.

3. Form of the RSTF.

In general, the RSTF is the joint characteristic function of the surface roughness $\chi(v_1, v_2; \bar{\Delta})$ evaluated along the diagonal $v_1 = v_z$; $v_2 = -v_z$. But since the composite surface given by (31) is desired, where ζ_{r_1} is the "waviness" component, and ζ_r is the "roughness" component, the RSTF (by (32)) is the product of the respective characteristic functions evaluated along the diagonal. For each roughness component ζ_{r_i} the RSTF is

$$\chi_1(v_z; \tau) = \exp \left[- \sigma_{s_i}^2 v_z^2 (1 - C_{s_i}(\tau)) \right]. \quad (39)$$

Extension to higher order surface composites ($n_s > 2$) is straightforward.

Depending on the size of the normalized surface variance

$$g_i = v_z^2 \sigma_{s_i}^2 \quad (40)$$

with respect to unity, the characteristic function χ_1 may be written two ways:

Case 1: For $g_i \ll 1$, the surface is slightly to moderately rough, and χ_1 in (39) is expanded in an exponential series which in general appears as:

$$e^z = \sum_{m=0}^{\infty} \frac{z^m}{m!} . \quad (41)$$

The plot of figure 10 gives the absolute error (ϵ) in approximating the infinite series (41) by the series which is truncated at m_1 , as a function of z . For example when $z = 0.1$, $m_1 = 3$ is sufficient for $\epsilon \leq 10^{-5}$. So

$$\chi_1(v_z; \tau) \approx e^{-g_1} \sum_{m=0}^{m_1} \frac{g_1^m}{m!} e^{-m(\tau/\tau_{o1})^2} . \quad (42)$$

Case 2: For $g_1 \gg 1$, the surface is very rough, and the characteristic function χ_1 is predominantly affected by C_{s_1} near unity (or τ near zero). Hence only the first two terms of the Maclaurin series for C_{s_1} are retained and

$$\chi_1(v_z; \tau) \approx \exp \left[-g_1 (\tau/\tau_{o1})^2 \right] . \quad (43)$$

This case should be used with caution, however, since for very rough surfaces the tangent plane approximation weakens.

4. Checking Boundary Conditions.

Finally, the initial assumptions of small slope and large radius of curvature are checked. The mean slopes ($\sqrt{2} \sigma_{s_1} / \tau_{o1}$ from eq. (106)) are found not to exceed 0.3 degrees for the waviness component and 1.0 degrees for the roughness component. Hence the small slope assumption is valid. To check for large radius of curvature, the one-dimensional curvature (K) is found point-wise on the computer for the samples using:

$$K(x) = \frac{d^2 \zeta}{dx^2} \left[1 + \left(\frac{d\zeta}{dx} \right)^2 \right]^{-3/2} . \quad (43a)$$

(Curvature is the inverse of the radius of curvature.) The probability density of K is found empirically, and the standard deviation σ_K is found from that density. Moments of the density of K are more meaningful than those of $1/K$ since in general the latter has a bimodal density and the former

a nearly monotonic density. The small curvature assumption is said to be valid if $\lambda \ll 1/\sigma_K$. In particular, $\sigma_K \leq 6.7 \times 10^{-3} \mu^{-1}$; hence $\lambda \ll 150 \mu$.

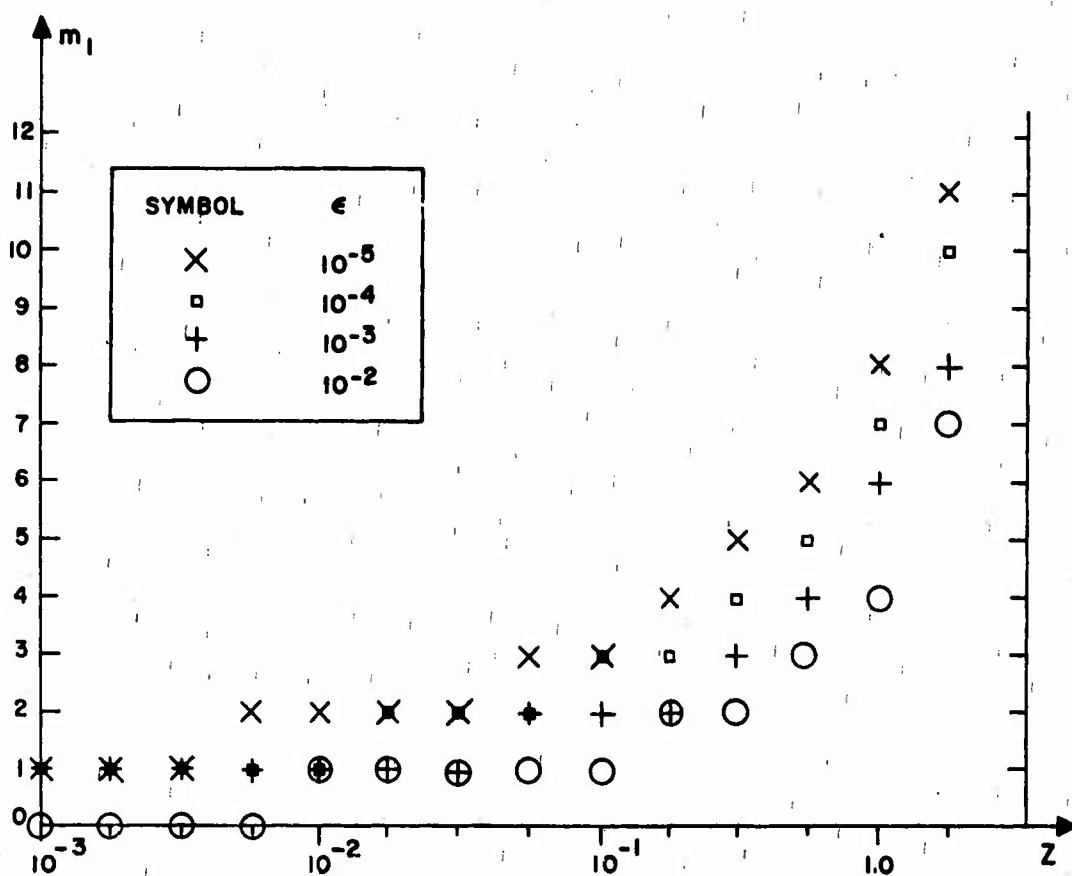


Figure 10. Summation limit m_1 versus argument z such that

$$\left| e^{\pm z} - \sum_{m=0}^{m_1} \frac{(\pm z)^m}{m!} \right| \leq \epsilon. \text{ For determining the number}$$

of terms needed to represent the diffuse component of scatter when $g_1 \approx 1$.

B. OPTICAL TRANSFER FUNCTION

In this section an OTF for the clear atmosphere is derived in a form suitable for the integration of (34). Such a solution is not only applicable to the scattering problem but more generally supplies the loss in coherence of a plane wave in the optical to infrared wavelengths propagated through the atmosphere. An alternate form for the OTF derived by Hufnagel and Stanley[12]

$$M(\rho) = \exp[-c\rho^{5/3}] \quad (44)$$

(where c is some constant) is perhaps accurate but prohibits closed-form integration of (34) since (44) is not analytic at the origin. Rather, an approximate Gaussian model:

$$C_o(\rho) = \exp[-c'\rho^2] \quad (45)$$

(c' a constant) is derived herein from the initial steps provided by Beran[13], [14] and Strohbehn [4], [15].

It is inappropriate here to reiterate Tatarski's work [3] on wave propagation in a turbulent medium. For our purposes, the most useful quantity presented by Tatarski is the three-dimensional spectral density of the index of refraction fluctuations as a function of wavenumber:

$$\Phi_n(\kappa) \sim \kappa^{-11/3}, \quad \kappa_o < \kappa < \kappa_m \quad (46)$$

assuming local isotropy and homogeneity. In (46), $\kappa_m = 5.92/\ell_o$ and $\kappa_o = 2\pi/L_o$ where ℓ_o and L_o are the inner and outer scales of turbulence, respectively. The outer scale (L_o) is usually taken [4] as the constant height above ground, and $\ell_o \sim 1$ to 10 mm. Strohbehn [4] has improved the form of Φ_n by rewriting the function to remove the singularity at the origin:

$$\Phi_n(\kappa) = \begin{cases} \alpha [1 + \kappa^2 L_o^2]^{-11/6} & \kappa \leq \kappa_m \\ 0 & \kappa > \kappa_m \end{cases} \quad (47)$$

$$\text{where } \alpha \approx \frac{C_n^2 L_o^{11/3}}{5.41 \pi^{3/2}} \quad (\kappa_m L_o \gg 1)$$

and C_n is the refractive index structure constant. Typical values for C_n^2

(for $L_0 < \text{a few hundred meters}$) given by Brown [16] range from $6 \times 10^{-13} \text{ m}^{-2/3}$ for the strongest daytime turbulence ($L_0 < \text{a few meters}$) to $6 \times 10^{-15} \text{ m}^{-2/3}$ for very weak turbulence at dawn or dusk. Actually, Strohbehn used a Gaussian taper function $\exp[-(\kappa/\kappa_m)^2]$ to turn off Φ_n at $\kappa = \kappa_m$. However, due to the low value of Φ_n at κ_m , form (47) is suitable here. As the wave-number κ decreases for $\kappa < \kappa_0$, the spectral density loses validity for two reasons: (a) The model presented by Strohbehn is only supposed to reduce the mathematical problems by removing the singularity at the origin. It does not necessarily fit experimental data for small κ . (b) For such small κ , the spectrum actually loses meaning since one may not assume homogeneity over very large separations in the corresponding structure function [3].

The OTF is found in terms of Φ_n by assuming the statistics of the wave amplitude ($|Z|$) are log normal and the wave phase ($\arg(Z)$) are normal. Experimental measurement [17],[18] and theoretical analysis [3], [4] using the central limit theorem have validated those assumptions. Beran [13],[14] and Strohbehn [4],[15] have derived the OTF in terms of the wave structure function (D) by somewhat independent procedures:

$$C_0(\Delta\xi, \Delta\eta) = \exp[-D(\Delta\xi, \Delta\eta)/2] \quad (48)$$

where $(\Delta\xi, \Delta\eta)$ are distances in the "incident system" (ξ, η) which is normal to the incident propagation vector \bar{k}_1 . (The wave structure function is the sum of Tatarski's log-amplitude and phase structure functions.) If, in addition to statistical homogeneity, isotropy is assumed, then $C_0 = C_0(\rho)$ where

$$\rho^2 = (\Delta\xi)^2 + (\Delta\eta)^2. \quad (49)$$

The wave structure function is related in general to the wave covariance (B_u) by

$$D(\rho) = 2(B_u(0) - B_u(\rho)). \quad (50)$$

If the wave correlation function $C_u(\rho) = B_u(\rho)/B_u(0)$, where $B_u(0)$ is the wave variance, then

$$C_0(\rho) = \exp[-B_u(0)(1 - C_u(\rho))]. \quad (51)$$

Note the formal similarity between (51) and the RSTF (39). In (51), $B_u(0)$ is a wave variance normalized to λ^2 , and in (39) $\sigma_{s_1}^2 v_z^2$ is a normalized surface variance. The reason for the similarity is that a joint characteristic function involving normal random variables is obtained as the RSTF; whereas a coherence of log-normal variables is the OTF.

The expression for the OTF in (48) and (51) is for an infinite plane wave Z . The results of this section are applicable to the scattering problem only if the separation $U = \ell Z$ in (33) is valid. In an independent approach based on Whitman and Beran [20], the decoupling is not assumed, and precisely the same scattering result (34) is derived. The reader can verify this by using an arbitrary boundary condition rather than Whitman's (3) and then evaluating the resulting coherence corresponding to his (22) at frequency $\bar{\mu} = \bar{0}$.

The correlation is written as a Fourier-Bessel transform of the spectrum $\Phi_n(\kappa)$:

$$C_u(\rho) = \frac{5 L_o^2}{3 \alpha} \int_0^\infty J_0(\kappa \rho) \Phi_n(\kappa) \kappa d\kappa \quad (52)$$

where J_0 is the Bessel function of first kind, zero order. At this point we note that since Φ_n for small κ loses validity, $C_u(\rho)$ for large $\rho (> L_o)$ is likewise questionable. Through straightforward integration the wave variance is found to be:

$$\begin{aligned} B_u(0) &= 4 \pi^2 k^2 R_o \int_0^\infty \Phi_n(\kappa) \kappa d\kappa \\ &= 0.786 k^2 R_o C_n^2 L_o^{5/3}. \end{aligned} \quad (53)$$

Equation (52) must be integrated numerically, except for small $\rho \ll \ell_o$ when

$$C_u(\rho) \approx 1 - \frac{5}{4} \left[(L_o \kappa_m)^{1/3} - \frac{6}{5} \right] (\rho/L_o)^2. \quad (54)$$

(Equations (52), (53), and (54) all assume $\kappa_m L_o \gg 1$.) Unfortunately, the absolute error in using (54) is less than or equal to $(\rho \kappa_m)^2$ per cent. Since the beam size is much greater than ℓ_o , form (54) is essentially useless. So computer integration is used to give a close approximation to $C_u(\rho)$:

$$C_u(\rho) \approx \exp[-1.125 (B_u(0))^{1/4} (\rho/L_o)^2], \quad \kappa_m \geq 3.3 (B_u^O(0))^{5/8} \quad (55)$$

where $B_u^O(0) = B_u(0) L_o^{-5/3}$ is not a function of κ_m and only depends on L_o to the extent that C_n does. The steps in deriving (55) are outlined in appendix II. For $\kappa_m < 3.3 (B_u^O(0))^{5/8}$, equation (54) is more appropriate than (55); however, (54) will be rarely needed except at long ranges or very short wavelengths. Furthermore, for $B_u(0) \gg 1$ (easily achieved), $C_o(\rho)$ in (51) is affected predominately by $C_u(\rho)$ near unity (i.e., for ρ near zero). Hence, only the first two terms of the Maclaurin series for $C_u(\rho)$ are kept in writing the OTF in the desired Gaussian form:

$$C_o(\rho) \approx \exp[-(\rho/\rho_o)^2] \quad (56)$$

$$\text{where } \rho_o = 0.945 (B_u^O(0))^{-5/8} L_o^{-1/24}. \quad (57)$$

For L_o less than a thousand meters, the e-folding length ρ_o can be approximated as

$$\rho_o \approx 1.1 (k^2 R_o C_n^2)^{-5/8}, \quad (58)$$

which is not quite dimensionally correct since the $L_o^{-1/24}$ factor has been dropped. Since $C_u(\rho)$ for ρ near zero is all that is needed in writing the OTF, the questionable character of $C_u(\rho)$ for large ρ is of no concern. Equation (58) says that the OTF of the atmosphere is only a function of wavelength, range, and the atmospheric structure constant.

It is now interesting to compare the above OTF with Hufnagel and Stanley's OTF [12]:

$$M(\rho) = \exp[-1.455 k^2 R_o C_n^2 \rho^{5/3}]. \quad (59)$$

A graphical comparison of (56) and (59) reveals only slight discrepancies, and indeed (56) is more suited for the closed-form integration of the mean power given by (34). In that integration, the independent variable ρ will be written in terms of the scattering coordinate system (x, y) rather than the incident system (ξ, η) using the isotropic distance ρ where

$$\rho^2 = (\Delta x \cos \theta_1)^2 + (\Delta y)^2. \quad (60)$$

Another OTF which may be of value to the reader was derived by Yura [19] for transmission through ocean water. He shows two mechanisms give rise to small-angle (less than 10^{-3} rad) forward light scattering: suspended biological particles with permittivity approximately that of water, and large-scale (with respect to λ) refractive index fluctuations. The OTF for the latter mechanism

$$M(\rho) = \exp[-(\rho/\rho_o)^2] \quad (60a)$$

$$\text{where } \rho_o = 2.76 (k^2 R_o C_n^2)^{-1/2} L_o^{1/6} \quad (60b)$$

is of course quite comparable to the atmospheric OTF in (56) and (57). Yura's notation has been changed for comparison with the present author's results. Note that Yura's variance of index of refraction fluctuations is $\overline{\Delta n^2} = 0.526 L_o^{2/3} C_n^2$. Initially it appears that the e-folding length of the OTF is larger in water than in the air -- a result which is not expected. However, this is not the case, since C_n^2 in water is typically about $3 \times 10^{-8} \text{ m}^{-2/3}$, much larger than in air. Notice it is a trivial matter to change from a calculation of scattering from a target in the atmosphere to scattering from the same target underwater. All that changes is the value of the "constant" ρ_o .

Because of the formal similarity of the OTF in (51) with the RSTF in (39), a rough surface with appropriate statistical characteristics can be used to simulate the turbulent atmosphere. Rather than transmit the wave through the atmosphere, the beam would be reflected at normal incidence from a rough surface (or transmitted through a random-phase transparency). The normally-distributed surface would have height variance $B_u(0) / (4 k^2)$, and the e-folding length of the Gaussian autocorrelation would be ρ_o . The surface would typically have a much larger variance and correlation length than the aluminum and titanium surfaces under study; hence the roughness could be formed by peening. Moreover, the mean slope $\sqrt{B_u(0)} / (\sqrt{2} k \rho_o)$ (from (106)) would not exceed about 1.0° (using $\lambda = 10.6 \mu$, $R_o = L_o = 1000 \text{ m}$, and $C_n^2 = 6 \times 10^{-14} \text{ m}^{-2/3}$), and so the tangent-plane approximation would still be valid. This is of course expected because the propagating medium cannot distort the phase of the wave so as to violate the original boundary conditions.

C. DETERMINISTIC TRANSFER FUNCTION

The DTF G_d is given by (24) where $V = \epsilon e^{iv_z \zeta_d}$. For the wave profile ϵ , the lowest order (TEM_{00}) circular output mode of the laser (assuming uniform spatial coupling at the output mirror) is taken in the scattering coordinate system:

$$\epsilon(x, y) = \epsilon_0 \exp \{ -[(x \cos \theta_1)^2 + y^2] / \ell^2 \} \quad (61)$$

where ℓ is the e-folding length of the electric (magnetic) field profile and ϵ_0 is the real amplitude factor. The e-folding length (ℓ') of the incident power is related to ℓ by $\ell = \ell' \sqrt{2}$.

The deterministic surface model is a quadric. In a coordinate system (u, v) which is rotated through an arbitrary angle η from (x, y) but in the same plane as (x, y) :

$$\zeta_d(u, v) = - \left(\frac{u^2}{2\rho_u} + \frac{v^2}{2\rho_v} \right) . \quad (62)$$

The transformation

$$(u, v) = (x \cos \eta - y \sin \eta, y \cos \eta + x \sin \eta) \quad (63)$$

is needed to write $\zeta_d(x, y)$. Relation (62) is the most general needed for a second-order surface since terms of lower order can be removed by rotation about the x or y axes. A rotation about the x -axis can be done arbitrarily since that merely redefines the incident polarization which has no effect here since $R = \pm 1$. That rotation would not be proper in the case of a non-perfect conductor, and hence first-order terms would be needed. A rotation about the y -axis can always be freely done since the incident angle θ_1 is with respect to the normal to the surface mean at the origin of the scattering system. However, rotation about the z -axis is not allowed since the orientation of this known surface (set by η) with respect to the incident (xz) plane cannot be changed at will.

If the exact surface can be adequately represented by terms to second order in its Maclaurin series, then the quadric surface (62) is

suitable. Such surfaces include a small area on a sphere, an ellipsoid, and a circular cylinder. In fact ρ_u (or ρ_v) is the radius of curvature of ζ_d taken along the v-axis (or u-axis) and then evaluated at the origin $u = 0$ (or $v = 0$). Moreover, the form in (62) will allow for closed-form integration for the DTF and the final power. Higher order terms of the expansion force computer integration.

Integration for the DTF yields the (anticipated) Gaussian form:

$$G_d(v_z; \bar{\Delta}) = \frac{A_o^2}{\cos \theta_1} \exp \left[-\frac{\rho^2}{2\ell^2} - \frac{v_z^2 \ell^2}{8} \left(\beta_1 (\Delta x)^2 + 2\beta_2 \Delta x \Delta y + \beta_3 (\Delta y)^2 \right) \right] \quad (64)$$

where $A_o^2 = \pi \ell^2 e_o^2 / 2$ is a pure constant formed for conservation of power. Namely $\frac{1}{2} Y_o A_o^2$ is the total power in the incident wave neglecting turbulence. Also

$$\beta_1 = \sec^2 \theta_1 \left(\frac{\cos^2 \eta}{\rho_u} + \frac{\sin^2 \eta}{\rho_v} \right)^2 + \sin^2 \eta \cos^2 \eta \left(\frac{1}{\rho_u} - \frac{1}{\rho_v} \right)^2$$

$$\beta_2 = -\sin \eta \cos \eta \left(\frac{1}{\rho_u} - \frac{1}{\rho_v} \right)$$

$$\left[\sec^2 \theta_1 \left(\frac{\cos^2 \eta}{\rho_u} + \frac{\sin^2 \eta}{\rho_v} \right) + \left(\frac{\sin^2 \eta}{\rho_u} + \frac{\cos^2 \eta}{\rho_v} \right) \right]$$

$$\text{and} \quad \beta_3 = \sec^2 \theta_1 \left(\frac{1}{\rho_u} - \frac{1}{\rho_v} \right)^2 \sin^2 \eta \cos^2 \eta + \left(\frac{\sin^2 \eta}{\rho_u} + \frac{\cos^2 \eta}{\rho_v} \right)^2. \quad (65)$$

Special cases including (a) a parabolic cylinder ($\rho_v \rightarrow \infty$), (b) a paraboloid of revolution ($\rho_u = \rho_v$), and (c) a flat plate ($\rho_u \rightarrow \infty$, $\rho_v \rightarrow \infty$) may be easily worked out if desired. For example if the mean surface is a flat plane, the DTF becomes the incident wave coherence:

$$G_d \Big|_{\zeta_d=0} = \frac{A_o^2}{\cos \theta_1} \exp \left(-\frac{\rho^2}{2\ell^2} \right). \quad (65a)$$

Hence the e-folding length of the incident wave coherence is $\sqrt{2} \ell$, of the incident field profile is ℓ , and of the incident power flux is $\ell/\sqrt{2}$. The

radii of curvature ρ_u and ρ_v may be either positive or negative; however, to justify the use of the tangent-plane approximation, $|\rho_u|$ and $|\rho_v|$ must be much greater than the wavelength and the beam size. Hence the scattering result (34) may not give the correct mean scattered power for every portion of the target surface -- especially if the beam size is large (e.g., one-fifth the length of the target), and the surface curvature is large (e.g., on a wing-tip).

D. FINAL INTEGRATED RESULT

The general result (34) with the three transfer functions (OTF (56,57), RSTF (32,39), and DTF (64)) substituted in is integrated to yield the expression for mean scattered power in closed form. Since Case 1 above ($g_i \leq 1$; $i=1,2$) is better suited to the original tangent plane approximation, and since the surfaces being studied are slightly to moderately rough, only the Case 1 expansion is necessary for each component of the rough surface. After integration of (34):

$$\langle\langle P_2 \rangle\rangle = \frac{A_o^2 |C_1|^2 Y_o}{2 \cos \theta_1} e^{-(g_1 + g_2)} \sum_{m=0}^{m_1} \sum_{n=0}^{n_1} \frac{g_1^m g_2^n}{m! n!} G(\bar{\gamma}; v_x, v_y) \quad (66)$$

where G is defined as a generalized two-dimensional Gaussian integral:

$$\begin{aligned} G(\bar{\gamma}; u, v) &= \int_{-\infty}^{\infty} \int_{-\infty}^{\infty} \exp \left[i(u\xi + v\eta) - (\gamma_1 \xi^2 + \gamma_2 \xi\eta + \gamma_3 \eta^2) \right] d\xi d\eta \\ &= \frac{2\pi}{\sqrt{4\gamma_1\gamma_3 - \gamma_2^2}} \exp \left(\frac{-u^2 \gamma_3 + uv\gamma_2 - v^2 \gamma_1}{4\gamma_1\gamma_3 - \gamma_2^2} \right) \\ &\quad (\gamma_1 > 0, \quad 4\gamma_1\gamma_3 > \gamma_2^2). \end{aligned} \quad (67)$$

In particular, the arguments γ for (66) are:

$$\gamma_1 = \left(\frac{1}{\rho_o^2} + \frac{1}{2\ell^2} \right) \cos^2 \theta_1 + \frac{m}{\tau_{o1}^2} + \frac{n}{\tau_{o2}^2} + \frac{v_z^2 \ell^2 \beta_1}{8}$$

$$\gamma_2 = \frac{v_z^2 \ell^2 \theta_2}{4}$$

$$\text{and } \gamma_3 = \left(\frac{1}{\rho_o^2} + \frac{1}{2\ell^2} \right) + \frac{m}{\tau_{o1}^2} + \frac{n}{\tau_{o2}^2} + \frac{v_z^2 \ell^2 \theta_3}{8} . \quad (68)$$

One further solution is written for the convenience of the reader -- that of a single component very rough surface (Case 2, $g \gg 1$; $n_s = 1$):

$$\langle\langle P_2 \rangle\rangle = \frac{A_o^2 |C_1|^2 Y_o}{2 \cos \theta_1} G(\bar{\gamma}; v_x, v_y) \quad (69)$$

where $\bar{\gamma}$ is as in (68), except let $n \rightarrow 0$, $m \rightarrow g$, and $\tau_{o1} \rightarrow \tau_o$.

Solutions of the form (66) and (69) are useful in computer programming the solution to the scattering problem but give little insight as to the mechanisms affecting the scattering behavior. Next, to reduce the complexity of the solution (66), typical values of the parameters of $\bar{\gamma}$ in (68) are investigated.

E. NUMERICAL RESULTS

The rough surface parameters were determined in the analysis outlined in section A of this chapter. For all the surfaces examined, $0.04 \leq \sigma_{s1} \leq 0.1 \mu$ ($i = 1, 2$); hence the roughness parameter $g_i \leq 2$ for $\lambda \geq 1.0 \mu$. This justifies the use of only Case 1 in the previous section, since the Nd-YAG ($\lambda = 1.06 \mu$) and the CO₂ ($\lambda = 10.6 \mu$) lasers are the most promising imaging sources. Except for very long ranges, very short wavelengths, or very small illuminated areas:

$$\frac{1}{\tau_{o1}^2} \gg \left(\frac{1}{\rho_o^2} + \frac{1}{2\ell^2} \right), \quad i = 1, 2.$$

(In fact, the definition of waviness and roughness components implies $\tau_{o1}^2 \gg \tau_{o2}^2$, but that assumption is not needed here.) Notice that if the wave were propagated underwater, ρ_o would be much smaller than in the atmosphere,

and the above assumption would not be applicable. (Refer back to (60b) and (58).) Furthermore, a flat mean ($\zeta_d = 0 = \theta_i$; $i=1,2,3$) is taken to reduce the complexity and to increase our understanding of the result.

The solution (66) is then separable into four significant terms:

$$\begin{aligned} \langle P_2 \rangle = & \frac{A_o^2 |C_1|^2 Y_o}{2 \cos \theta_1} e^{-(g_1+g_2)} \left\{ A \exp \left[- \frac{A \cos \theta_1}{4 \pi} \left(\left(\frac{v_x}{\cos \theta_1} \right)^2 + v_y^2 \right) \right] \right. \\ & + \tau_{o1}^2 \pi \sum_{m=1}^{m_1} \frac{g_1^m}{m! m} \exp \left[- \tau_{o1}^2 v_{\perp}^2 / (4m) \right] + \tau_{o2}^2 \pi \sum_{n=1}^{n_1} \frac{g_2^n}{n! n} \exp \left[- \tau_{o2}^2 v_{\perp}^2 / (4n) \right] \\ & \left. + \pi \sum_{m=1}^{m_1} \sum_{n=1}^{n_1} \frac{g_1^m g_2^n}{m! n! \left(\frac{m}{\tau_{o1}^2} + \frac{n}{\tau_{o2}^2} \right)} \exp \left[- v_{\perp}^2 / \left(4 \left(\frac{m}{\tau_{o1}^2} + \frac{n}{\tau_{o2}^2} \right) \right) \right] \right\} \quad (70) \end{aligned}$$

where $v_{\perp}^2 = \bar{v}_{\perp} \cdot \bar{v}_{\perp}$, and an effective area of illumination is defined as

$$A = \pi \left[\cos \theta_1 \left(\frac{1}{2 l^2} + \frac{1}{\rho_o^2} \right) \right]^{-1}. \quad (71)$$

In the special case of no turbulence ($\rho_o \rightarrow \infty$) and a flat mean ($\zeta_d = 0$), the effective area is the total integral of the incident coherence ($A_o^2 2 l^2 \pi / \cos^2 \theta_1$) divided by the peak incident coherence ($A_o^2 / \cos \theta_1$). (The incident coherence is given in general by (35) and for a Gaussian profile by (65a).) Alternatively the area A is the area of an ellipse with semi-axes equal to the e-folding lengths in the Δx and Δy directions of the incident coherence ($\sqrt{2} l / \cos \theta_1$ and $\sqrt{2} l$, respectively).

The first term in (70) is defined as the coherent (or specular) scatter since it is the observed scatter from a perfectly flat plate (i.e., $g_1 = g_2 = 0$). The second term is the primary diffuse scatter due to the surface waviness component; third is the primary diffuse term due to the surface roughness component; and the double summation is a remaining contribution due to all surface roughness. If $g \ll 0.25$ (where $g = g_1 + g_2$), then the double summation in (70) is negligible. In that case we can let $n_1 = m_1 = 1$ since

the absolute truncation error will not exceed 10^{-3} (obtained from figure 10 for $g = 0.2$). Hence, if $g \ll 0.25$:

$$\begin{aligned} \langle\langle P_2 \rangle\rangle \approx & \frac{A_o^2 |C_1|^2 Y_o}{2 \cos \theta_1} e^{-g} \left\{ A \exp \left[-\frac{A \cos \theta_1}{4 \pi} \left(\left(\frac{v_x}{\cos \theta_1} \right)^2 + v_y^2 \right) \right] \right. \\ & \left. + \pi \tau_{o_1}^2 g_1 \exp \left[-\tau_{o_1}^2 v_{\perp}^2 / 4 \right] + \pi \tau_{o_2}^2 g_2 \exp \left[-\tau_{o_2}^2 v_{\perp}^2 / 4 \right] \right\}. \quad (72) \end{aligned}$$

Equation (72) is appropriate for the CO_2 laser wavelength, 10.6μ , since $g \leq 0.02$ for the titanium and aluminum under examination. However, if the Nd-YAG laser is used, $\lambda = 1.06 \mu$, $g \leq 2.$, and all the terms in (70) must be retained. (The summations could terminate at $n_1 = m_1 = 8$ for an error less than 10^{-3} .)

Note that in (71) an increase in turbulence (ρ_o decreasing) implies a decrease in effective area A . Consequently the coherent component widens, and its peak decreases. Most important, the coherent term is affected by both the wave profile (via t) and the turbulence (via ρ_o); whereas the diffuse terms depend only on surface parameters (τ_{o_1} and σ_{s_1}). If the turbulence had been much stronger (say for a wave propagated underwater), then ρ_o would have influenced the diffuse terms rather than the coherent. The expression for such a case will not be shown since it is taken care of by (66). When the surface becomes rougher (by increasing g), power is coupled from the coherent component to the diffuse. That decrease in the coherent component is accounted for by the $\exp[-g]$ factor which multiplies the entire expression. It is observed that variable β_1 (and hence a variable deterministic surface ζ_d) will affect either the diffuse or the coherent terms, or both, for typical β_1 . If such values are to be included, then one should either use the general expression (66) or, based on the actual values of β_1 , decide whether the known surface affects the diffuse or the coherent terms in (70).

To give further feel for the scattering expression (70), sample scattering patterns at the CO_2 laser wavelength are given in figure 11 for titanium and figure 12 for aluminum. The condition of turbulence is weak

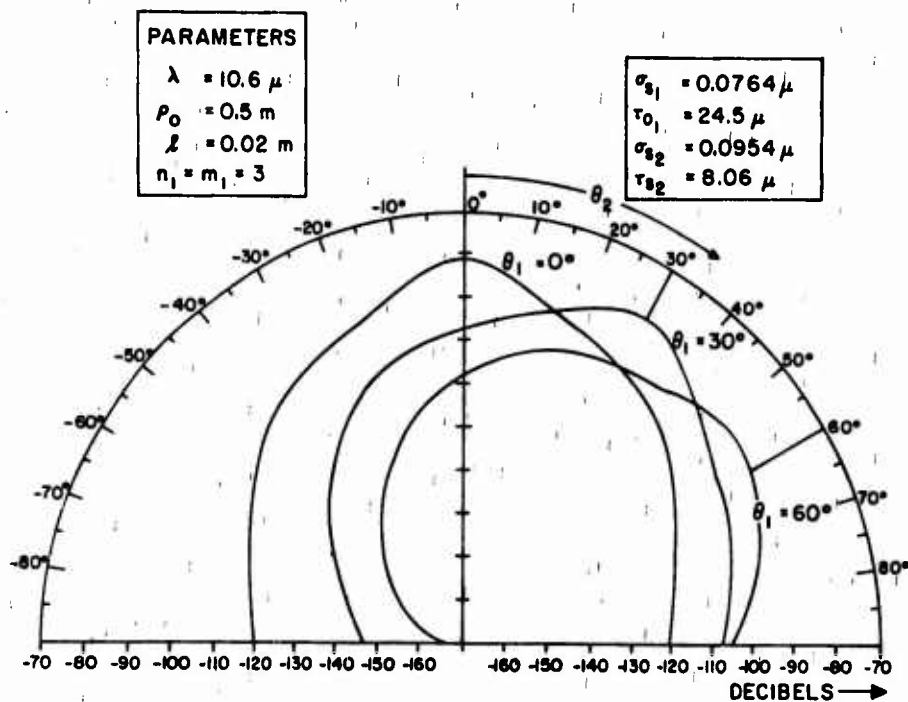


Figure 11. Polar plots of mean scattered power (in db) for $\theta_3=0$, θ_1 = constant, θ_2 varied; normalized to power at $\theta_1=\theta_2=\theta_3=0$. Parameters for titanium found in surface tracing.

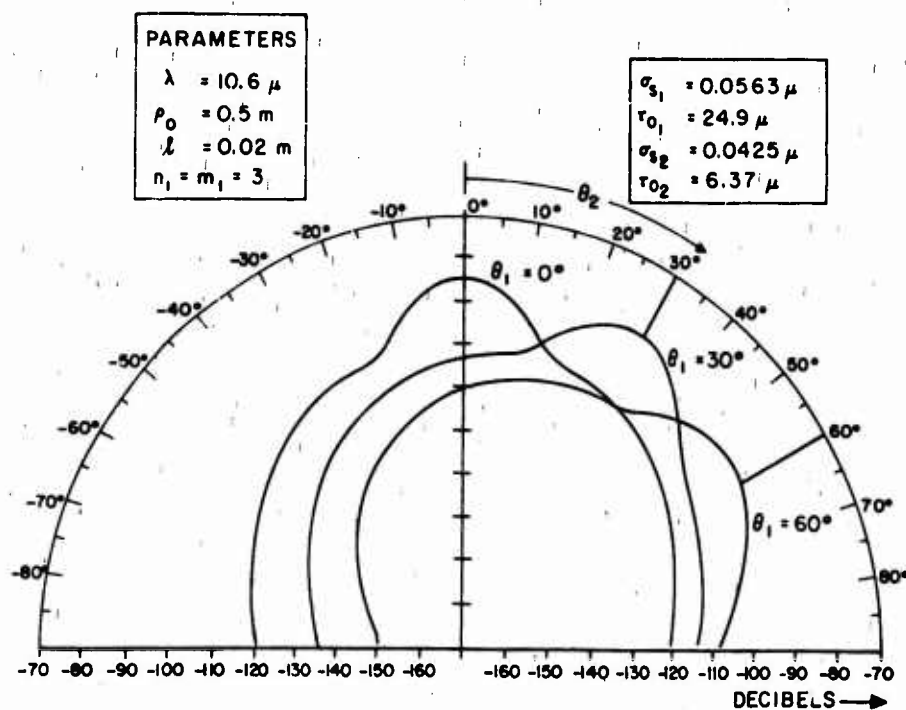


Figure 12. Polar plots of mean scattered power. Same conditions as figure 11 but for aluminum parameters.

($C_n^2 = 6 \times 10^{-15} \text{ m}^{-2/3}$, $R_o = 250 \text{ m}$) so that the individual components of scatter may be discerned. The polar plots of scattered power are in decibels where the reference power is the backscattered power at normal incidence. (Hence the norm is not a function of $(\theta_1, \theta_2, \theta_3)$ but does depend on the system parameters l, ρ_o, τ_{o_i} , and σ_{s_i} .) For each incident angle ($\theta_1 = 0^\circ, 30^\circ, 60^\circ$), the widest and next-to-widest lobes are the diffuse scatter due to roughness and waviness respectively. The extremely narrow lobe is the coherent component. In practice wider coherent components are encountered because of stronger turbulence and because of an incident spherical wave. All reasonable degrees of turbulence are taken care of by (70); how to account for an incoming spherical wave is the subject of the next section, part 1.

F. SPECIAL CASES

In this section we give further interpretation of the scattering result (70) by investigating special cases. Actually the first case extends (70) by introducing incident waves with slight spherical character. Second, in the special case of zero mean ($\zeta_d = 0$), equation (70) reduces to Beckmann's result. Third, the direct backscatter case is analyzed to show more closely the way roughness parameters affect scattering behavior. Finally, scatter from a perfectly smooth surface is presented. All cases are tied closely together, and the reader will note some conclusions apply to many special cases.

1. Incident Spherical Waves.

As pointed out in the examples of scatter in figures 11 and 12, the coherent component of scatter is often much wider than predicted for an incident plane-wave. The reason in part is that the incident wave must always possess some spherical (or second-order) curvature. To account for this, we do not have to go back to the Helmholtz integral and rewrite the expression for incident fields. Rather, the deterministic surface is deformed spherically with radius of curvature twice that of the radius of the incident wave-fronts. If the incident divergence angle is α_o (between e-folding points

of the incident field), then $\eta = 0$, $\rho_v = 4\ell/\alpha_o$, and $\rho_u = \rho_v/\cos\theta_1$. Hence $\beta_1 = \beta_2 = [\alpha_o/(4\ell)]^2$, $\beta_2 = 0$ is substituted in $\bar{\gamma}$, eq. (68). As a result, the revised coherent term (first in the brace of (70)) becomes

$$\frac{\pi}{\sqrt{\gamma'_1 \gamma'_3}} \exp \left[-\frac{1}{4} \left(\frac{v_x^2}{\gamma'_1} + \frac{v_y^2}{\gamma'_3} \right) \right] \quad (73)$$

where $\gamma'_1 = \left(\frac{1}{\rho_o^2} + \frac{1}{2\ell^2} \right) \cos^2\theta_1 + \frac{v_z^2 \alpha_o^2}{128}$

and $\gamma'_3 = \left(\frac{1}{\rho_o^2} + \frac{1}{2\ell^2} \right) + \frac{v_z^2 \alpha_o^2}{128}$

provided $\alpha_o^2 \ll (\lambda/\tau_{o_i})^2$, $i=1,2$.

To demonstrate the significance of including an incident spherical wave, suppose $\rho_o = 10$ cm, $\ell = 1$ cm, $\alpha_o = 1$ mrad, and $\lambda = 10^{-5}$ m. Then $1/(2\ell^2) = 5 \times 10^3 \text{ m}^{-2}$ and $(v_z \alpha_o)^2/128 \leq 1.25 \times 10^4 \text{ m}^{-2}$. In this typical example, turbulence is negligible, but the spherical wave is as important as the wave profile contribution.

2. Normalized Power, Compared With Beckmann.

The normalized expression for mean scattered power is shown to agree with Beckmann's result [1] in the special case of a zero-mean rough surface ($\zeta_d = 0$), a single-component rough surface model ($n_s = 1$), and a perfectly plane incident wave ($\alpha_o = 0$). Normalization is with respect to backscatter at normal incidence from a perfectly smooth surface. The area A defined by (71) is especially constructed to correspond to Beckmann's area $4 L_x L_y$, where $2 L_x$ and $2 L_y$ are the sides of the uniformly illuminated rectangular surface. Since turbulence is lumped into the effective area A , it is not necessary to require no turbulence in the comparison. The normalized expression is:

$$p = F_3^2 e^{-g} \left\{ \exp \left[-\frac{A \cos \theta_1}{4\pi} v'^2 \right] + \frac{\tau_o^2 \pi}{A} \sum_{m=1}^{m_1} \frac{g^m}{m! m} \exp \left[-\tau_o^2 v_{\perp}^2 / (4m) \right] \right\} \quad (74)$$

where $v'^2 = \left(\frac{v_x}{\cos \theta_1} \right)^2 + v_y^2$,

$$g = (v_z \sigma_s)^2,$$

and $F_3 = \left[1 - \frac{v_x}{v_z} \tan \theta_1 \right]$.

Beckmann's expression (eq. (57), p. 88 in [1]) can be achieved if the notation is revised by

$$\tau_o \rightarrow T,$$

$$v_{\perp}^2 \rightarrow v_{xy}^2,$$

$$m_1 \rightarrow \infty,$$

and $F_3^2 \exp \left[-\frac{A \cos \theta_1}{4\pi} v'^2 \right] \rightarrow \rho_o^2$.

The last expression is the normalized coherent component of scatter (the scatter from a perfectly smooth surface replacing the rough one).

3. Direct Backscatter.

When an image is formed by scanning the source beam over the target, a large amount of backscattered power is needed for all incident angles. To investigate how the power in direct backscatter can be increased, the power as given by (70) (at $\theta_2 = -\theta_1$; $\theta_3 = 0$) is normalized to the backscattered power at normal incidence (a pure number) by:

$$\langle \langle P_2 \rangle \rangle_B = \langle \langle P_2 \rangle \rangle \Big|_{(\theta, -\theta, 0)} / \langle \langle P_2 \rangle \rangle \Big|_{(0, 0, 0)}. \quad (75)$$

To simplify the analysis, we take only a single-surface model ($n_s = 1$). Then

$$\langle \langle P_2 \rangle \rangle_B = (\sec^4 \theta) \exp [(2 k \sigma_s \sin \theta)^2] \left\{ \exp \left[-\frac{Ak^2}{\pi} \sin \theta \tan \theta \right] + \frac{\tau_o^2 \pi}{A} \sum_{m=1}^{m_1} \frac{(\sigma_s^2 2 k \cos \theta)^{2m}}{m! m} \exp \left[-\frac{(\tau_o k \sin \theta)^2}{m} \right] \right\}. \quad (76)$$

If $k \tau_o$ is decreased, the surface roughens because the peaks come closer together relative to the wavelength. Hence the diffuse scatter widens. Since we have no control over τ_o , we must increase the wavelength to increase backscattered power at the large angles, θ . Unfortunately, a decrease in $k \tau_o$ causes a decrease in the peak (at $\theta=0$) and total power of the diffuse component. So there is a trade-off between desired width and peak. In addition, an increase in surface variance σ_s^2 will increase diffuse backscatter overall. An analysis similar to the above can be performed if the imagery is effected at some bistatic angle (i.e. receiver not located at laser source); yet monostatic imagery gives us the required information on the effect of surface parameters on the diffuse scatter. Sample backscatter plots using the aluminum and titanium parameters are provided in figure 13. These plots and those of figures 11 and 12 are generated on a digital computer using the composite result (70). Because of the low level power in the diffuse scatter, it is readily obvious that receiver electronics, laser power, and detector sensitivity will have to be quite good to detect backscattered power for angles significantly different from the specular.

4. Scatter From a Perfectly Smooth Surface.

In order to provide a heuristic verification of the coherent component in (70), the scatter from a perfectly smooth surface for vertical incidence, when there is no turbulence present, is investigated. The normalized coherent component of (74) for $\rho_o \rightarrow \infty$ is:

$$p_c \approx \exp [-(\theta_2 / \theta_{20})^2] \quad (77)$$

$$\text{where } \theta_{20} = \frac{2}{k} \left(\frac{1}{2i^2} + \frac{k^2 \alpha_o^2}{32} \right)^{\frac{1}{2}} \quad (78)$$

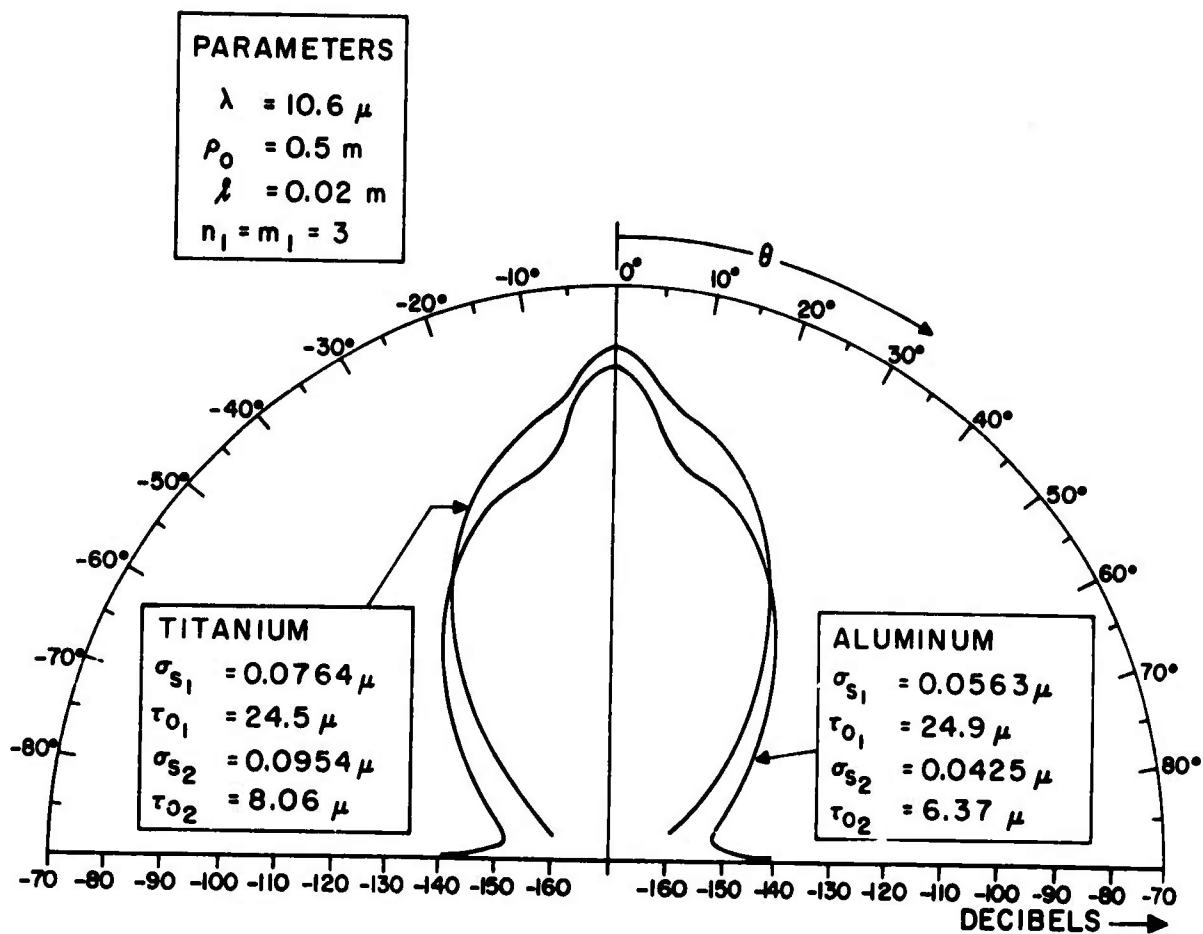


Figure 13. Polar plots of mean backscattered power (in db) for $\theta_3 = 0$,
 $\theta = \theta_1 = -\theta_2$ varied; normalized to power at $\theta_1 = \theta_2 = \theta_3 = 0$.

is the e-folding angle ($\theta_{20} \ll \pi/2$ assumed). Suppose divergence dominates profile:

$$\frac{1}{2 \ell^2} \ll \frac{k^2 \alpha_0^2}{32} . \quad (79)$$

Then the e-folding angle is the same as the e-folding angle of the incident power:

$$\theta_{20} = \frac{\alpha_0}{\sqrt{8}} . \quad (80)$$

(Recall α_0 is the total divergence angle measured between e-folding points on the incident field profile.) Now suppose profile dominates divergence:

$$\frac{1}{2 \ell^2} \gg \frac{k^2 \alpha_0^2}{32} . \quad (81)$$

Then

$$\theta_{20} = \frac{\sqrt{2}}{k \ell} . \quad (82)$$

This compares favorably with the half-angle divergence $1.36/(k\ell)$ of a uniform beam diffracted by a round pin-hole of diameter $4\sqrt{2} \ell$. Hence for both the special cases of the coherent scatter, the solution reduces to well-known results of diffraction theory.

G. THE INVERSE PROBLEM

1. Scatter at Normal Incidence.

The subsequent analysis demonstrates how to determine the surface power spectral density and the atmospheric refractive index structure constant from a measurement of scattered power where the wave is normally incident on the surface ($\theta_1 = 0$). All the assumptions used in the modeling apply here except we assume no knowledge of the surface power spectrum. One additional restriction is that the surface is only slightly rough:

$$k^2 \sigma_s^2 \ll 1 , \quad (83)$$

where σ_s^2 is the rough surface variance. Recall that of all the aspects of modeling, a form for P_s was never theoretically derived. Rather, a sum of

two Gaussians was determined experimentally to be a good approximation. Once again, the assumptions of statistical isotropy and homogeneity for a normally distributed surface are applied. If those assumptions are valid, then a measurement of the surface power spectrum gives a complete second-order statistical description of the surface. Since this method determines properties of the surface and the medium from scatter measurements, the analysis is referred to as the "inverse problem." Not only are these results valuable in studying surfaces at large ranges, but also in getting a quick statistical description of a surface in a laboratory. There is less error involved in this passive probe since most surface tracing devices physically deform the surface.

The revised expression for normalized mean scattered power (for $\theta_1=0$) is once again a sum of a coherent (p_c) and a diffuse term (p_d):

$$\begin{aligned} p(\theta_2) &= p_c + p_d \\ &= \exp \left[-\frac{A' v^2}{4\pi} \right] + \frac{v_{zo}^2}{A'} \int_0^\infty B_s(\tau) J_0(v\tau) \tau d\tau \end{aligned} \quad (84)$$

where $A' = \pi \left[\frac{1}{2l^2} + \frac{1}{\rho_o^2} + \frac{k^2 \alpha_o^2}{32} \right]^{-1}$,

$$v = k \sin \theta_2,$$

and $v_{zo}^2 = k^2 (1 + \cos \theta_2)^2$.

The surface covariance $B_s(\tau) = \sigma_s^2 C_s(\tau)$ is assumed to drop to a value much less than σ_s^2 in a distance $\tau \ll \sqrt{A'/\pi}$, and that the e-folding angle of the coherent component is much less than $\pi/2$. The Fourier-Bessel transform in (84) is achieved because of vertical incidence and because of the isotropy of the rough surface and the atmosphere. Normal incidence makes the three transfer functions dependent on τ rather than some being functions of ρ .

The coherent term in (84) gives the information on the atmosphere by relating ρ_o , the e-folding length of the OTF, to the measurable coherent component of scatter. The e-folding angle of the coherent component θ_{20}

is related to A' through

$$\theta_{20} = \frac{2}{k} \sqrt{\frac{\pi}{A'}} \quad (85)$$

Rearranging equation (85) we find:

$$\rho_o = \left[k^2 \left(\frac{\theta_{20}^2}{4} - \frac{\alpha_o^2}{32} \right) - \frac{1}{2\ell^2} \right]^{-\frac{1}{2}} \quad (86)$$

Finally, the refractive index structure constant C_n is related to ρ_o via equation (58) or

$$C_n^2 = \frac{(\rho_o / 1.1)^{-8/5}}{R_o k^2} \quad (87)$$

Hence the strength of turbulence can be measured by measuring the e-folding angle of the coherent scatter (assuming we know R_o , k , α_o , and ℓ).

From the diffuse component of scatter p_d in (84), we can find the surface power spectral density (and hence the variance and autocorrelation). Since the surface two-dimensional power spectral density V_s is the Fourier-Bessel transform of the covariance (see appendix III), then by direct comparison with diffuse component in (84):

$$V_s(v) = \frac{A' p_d(v)}{2\pi v_{z0}^2} \quad (88)$$

Hence to obtain V_s , the diffuse scatter $p_d(\theta_2)$ is scaled by the factor $A'/(2\pi v_{z0}^2)$, and the abscissa is converted from θ_2 to $k \sin \theta_2$. Because of isotropy of statistics, the relation is independent of θ_3 and requires a measurement of scattered power for $0 \leq \theta_2 < \pi/2$ for any θ_3 . Even though $V_s(v)$ has non-zero values for $v > k$ (where $v = k$ is the limit of measurement), we must make some assumption on the character of $V_s(v > k)$. Either $V_s(v > k)$ is set to zero, or it is set by some trend (e.g. Gaussian) which is established for $v < k$.

In appendix III, the one-dimensional power spectral density P_s is related to V_s by

$$P_s(\kappa) = \int_{\kappa}^{\infty} \frac{2v}{\sqrt{v^2 - \kappa^2}} V_s(v) dv \quad (89)$$

where $\kappa = 2\pi v$. (The only restriction on V_s is that it be Bessel-transformable.) Unfortunately the transform in (89) does not possess an inverse which is a single-variable integral, and tables for this transform have not been generated. Hence the most straightforward way to go from V_s to P_s is to Fourier-Bessel transform V_s , and then Fourier-cosine transform the result. To go from P_s to V_s , the procedure is reversed. There is one caution in getting V_s from P_s : that the Fourier-cosine transform of P_s must be Bessel-transformable. This immediately eliminates the Dirac-delta function (for P_s) which possesses a non-convergent Fourier-cosine transform. However, if V_s is a delta function of area $2c$:

$$V_s(v) = c [\delta(v - v_1) + \delta(v + v_1)] \quad (90)$$

then

$$P_s(\kappa) = \begin{cases} \frac{2cv_1}{\sqrt{v_1^2 - \kappa^2}} & |\kappa| \leq v_1 \\ 0 & |\kappa| > v_1 \end{cases} \quad (91)$$

This says that information stored as a delta function at $v = \pm v_1$ in V_s affects the character of $P_s(\kappa)$ for $|\kappa| \leq v_1$, but not for $|\kappa| > v_1$.

Relations (90) and (91) show how to choose a suitable Nyquist frequency when $P_s(v)$ is measured by a surface tracing method (e.g. on a proficorder). The maximum value on the abscissa of V_s is $v = k$ (since $|\theta_2| < \pi/2$). In the abscissa of P_s , that maximum corresponds to $v = 2\pi k = \lambda^{-1}$. Hence for a scatter measurement for all θ_1 (rather than just $\theta_1 = 0$), a suitable Nyquist frequency is

$$v_{NY} = 2\lambda^{-1}. \quad (92)$$

(Namely the sampling period would be $\lambda/4$ or shorter.) Alternatively, a determination of P_s via a scatter measurement can be made for frequency v greater than physically possible with the most sensitive surface tracing devices. For example, generally on the best proficorder surface trace, a

minimum reasonable sampling period is about 0.1 mil (which corresponds to a Nyquist frequency of $0.196 \mu^{-1}$). However, for a Nd-YAG laser beam ($\lambda = 1.06 \mu$) scattered from the same surface (at normal incidence), the Nyquist frequency is $0.943 \mu^{-1}$. (Of course, inequality (83) must still be satisfied.)

To see how to use equations (88) and (89), we look at a concrete example by returning to the Gaussian model for the one-dimensional power spectrum:

$$P_s(v) = \sigma_s^2 \tau_o \sqrt{\pi} \exp[-(v \pi \tau_o)^2]. \quad (93)$$

(A one-surface model, $n_s = 1$, is sufficient for explanatory purposes and can easily be extended to higher orders.) Hence we find

$$p_d(v) = \frac{\pi \tau_o^2 \sigma_s^2 v^2}{A'} \exp[-(\tau_o v / 2)^2]. \quad (94)$$

If the Gaussian model is appropriate for P_s , the surface parameters σ_s and τ_o can be found from a quick examination of the scatter pattern. Initially, the peak of the diffuse component $p_d(0)$ gives

$$(\sigma_s \tau_o)^2 = \frac{p_d(0) A'}{4 k^2 \pi}. \quad (95)$$

(The A' is found in the analysis of the coherent component.) Secondly, suppose the e-folding angle of $p_d(\theta_2)$ is θ_{20}' , and that $\theta_{20}' \leq \pi / 4$. Then to a close approximation

$$\tau_o = \frac{2}{k \theta_{20}'} \quad (96)$$

and of course (96) in (95) gives σ_s . We can extend this procedure to higher-order composite surfaces by examining each component of scatter individually (provided the components are distinguishable). The e-folding angles of the coherent and diffuse components (assuming (93) is the power spectrum) are depicted in the hypothetical scatter plot of figure 14.

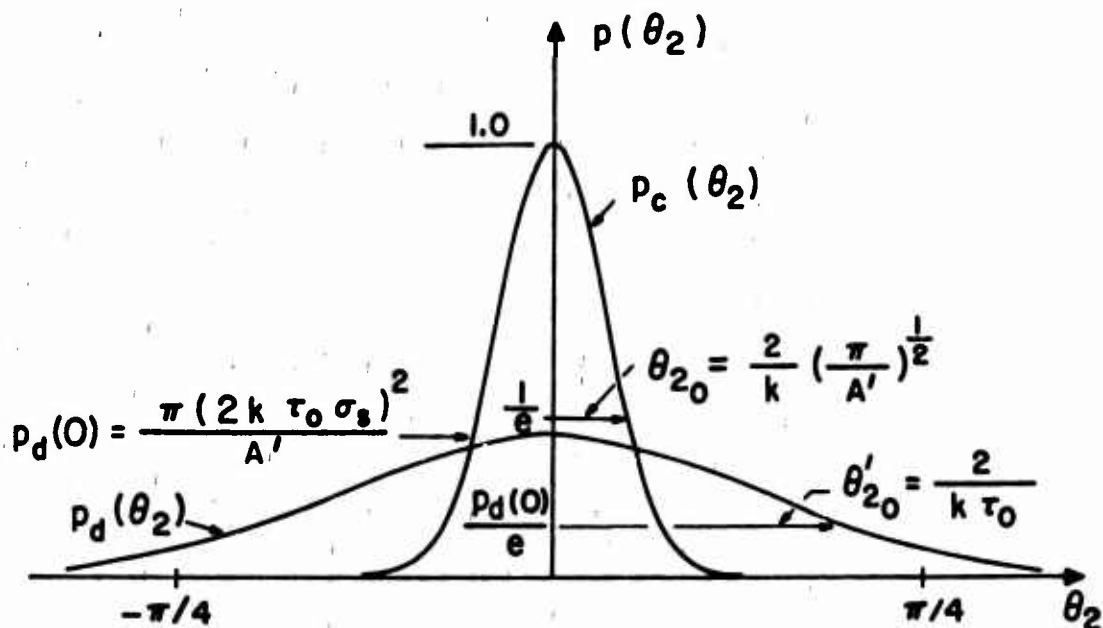


Figure 14. Hypothetical scatter at normal incidence from a slightly rough surface with Gaussian p.s.d.f. and p.d.f. showing relation between e-folding widths and peaks of components.

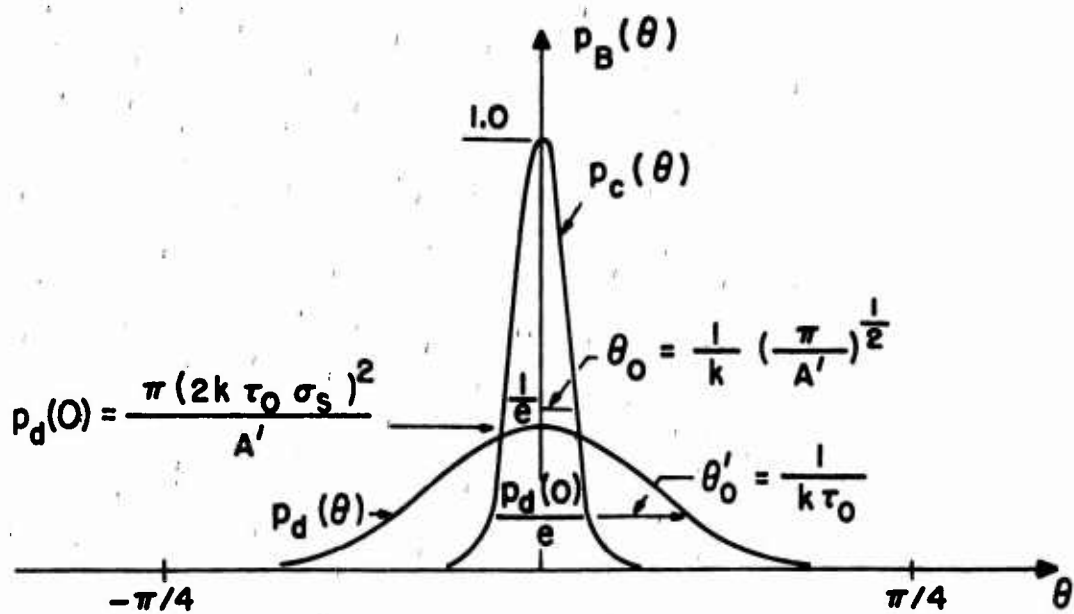


Figure 15. Hypothetical backscatter (otherwise like figure 14).

2. Direct Backscatter.

There is, however, another measurement which can be made to give ρ_o , τ_o , and σ_s and in some cases the surface power spectral density. If instead of the scatter for vertical incidence being measured, suppose that the direct backscatter from the surface ($\theta=\theta_2=-\theta_1$, $\theta_3=0$) is a more convenient measurement. The expression analogous to (84) is

$$p_B(\theta) = \exp \left[-\frac{A' v^2}{\pi} \right] + \frac{4 k^2 \sec \theta}{A'} \iint_{-\infty}^{\infty} B_s(\tau) e^{i 2 v x} dx dy. \quad (97)$$

Unfortunately (97) does not provide us a means of finding a general $B_s(\tau)$ from $p_B(\theta)$. If however, the covariance can be decoupled as

$$B_s(\tau) = \sigma_s^2 C_{s1}(x) C_{s1}(y), \quad (98)$$

then the covariance can be found from a measurement of diffuse power, $p_d(\theta)$ (the second term in (97)). If we define the Fourier-cosine transform

$$I(x) = \int_0^{\infty} (\cos \theta) p_d(\theta) \cos(2 v x) dv \quad (99)$$

$$\text{then } C_{s1}(x) = I(x) / I(0) \quad (100)$$

$$\text{and } B_s(\tau) = \frac{A' I(x) I(y)}{4 \pi k^2 \int_0^{\infty} I(x) dx} \quad (101)$$

From the covariance, either the one or two-dimensional power spectral densities can be found (as Fourier-cosine or Fourier-Bessel transforms of $B_s(\tau)$, respectively). As in the case of scatter for normal incidence, the constant A' is found from the coherent component of scatter, $p_c(\theta)$ (first term in (97)). If the e-folding angle of the coherent component, θ_o , is much less than $\pi/2$, then

$$A' = \frac{\pi}{k^2 \theta_o^2} \quad (102)$$

Moreover, the e-folding length of the OTF is

$$\rho_o = \left[k^2 \left(\theta_o^2 - \frac{\alpha_o^2}{32} \right) - \frac{1}{2\ell^2} \right]^{-\frac{1}{2}}, \quad (103)$$

and C_n^2 is found from (87). If in addition the Gaussian model (93) for P_s is assumed, and the e-folding angle of the diffuse component of scatter, θ'_o , is less than about $\pi/4$, then to a close approximation:

$$\tau_o = (k \theta'_o)^{-1} \quad (104)$$

$$\text{and } (\sigma_s \tau_o)^2 = \frac{p_d(0) A'}{4 k^2 \pi}. \quad (105)$$

The e-folding angles and peaks of the diffuse and coherent components are depicted in figure 15. From a direct comparison of figures 14 and 15, we see that backscatter $p_B(\theta)$ is exactly the same as the direct scatter with its abscissa compressed by a factor of two, $p(2\theta_2)$. This conclusion does not apply in general but is at least valid for a Gaussian power spectral density. Extension to higher order surface composites is straightforward provided the individual components are distinguishable.

Chapter IV

EXPERIMENTAL RESULTS

This chapter presents measurements of scattering of a CO_2 laser beam from the aluminum and titanium surfaces which were analyzed on the proficorder. The turbulence is assumed negligible, and the surfaces have a zero mean; hence the comparison of experimental results and theoretical computer-generated curves will serve as a verification of the rough surface and profile aspects of the theory. In addition, this checks the accuracy of the composite-surface model. There are four patterns of scatter in the plane of incidence ($\theta_3 = 0$) presented: scatter from titanium for $\theta_1 = 27^\circ$ and 3.5° , and from aluminum for 18° and 3.5° . (The beam was incident upon the location where proficorder traces were made.) The data for the near-normal incidence ($\theta_1 = 3.5^\circ$) are also used to derive the surface P_s via the procedure of the "inverse problem." (Achieving $\theta_1 = 0$ is physically impossible in the present experimental set-up.) As a further check of the rough surface model, the power spectrum P_s^s (super-s to indicate originated from a scattering measurement) is compared with P_s^t (super-t for proficorder trace).

A. EXPERIMENTAL ARRANGEMENT

This section outlines the apparatus used in making the scatter measurements. (See figure 16.) The CO_2 laser beam passes through a beam splitter (for monitoring laser power on the thermopile), through a chopper wheel (for lock-in amplification), and is reflected to the scattering surface mounted on the target table. All components are adjusted until the laser beam, the normal direction to the surface, and the detector are coplanar. The maximum distance from target to detector is 50 cm; and a lens at the detector increases signal strength. The detector is mounted on an optical bench which is rotated manually about the scattering surface. Below the bench is a pointer which indicates the scattering angle θ_2 with accuracy better than $\pm \frac{1}{4}$ degree. The major system components-- the laser and its monitor, the detector and its

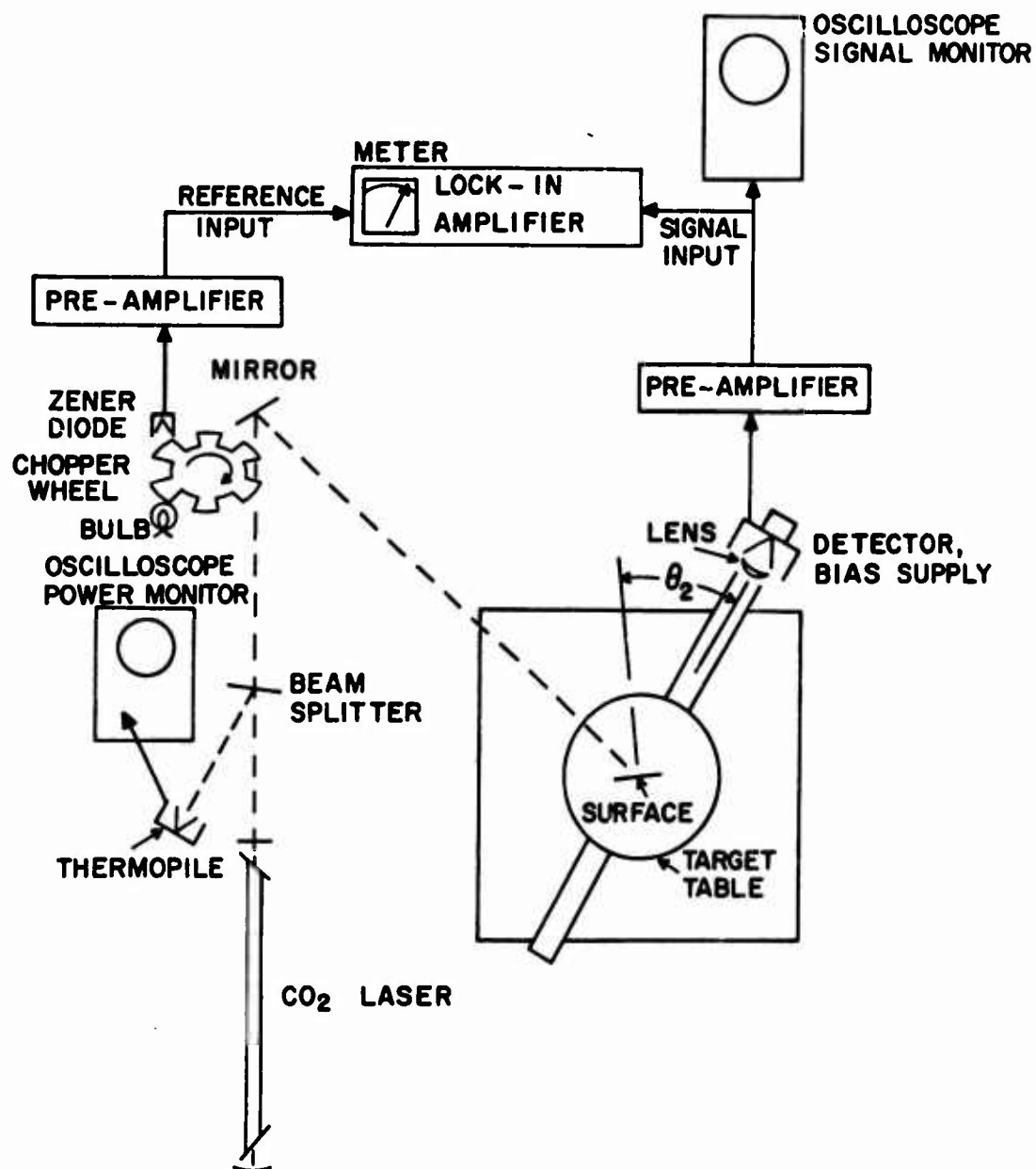


Figure 16a. Experimental set-up for measurement of scattered power versus θ_2 when $\theta_3 = 0$ and θ_1 is set.

NOT REPRODUCIBLE

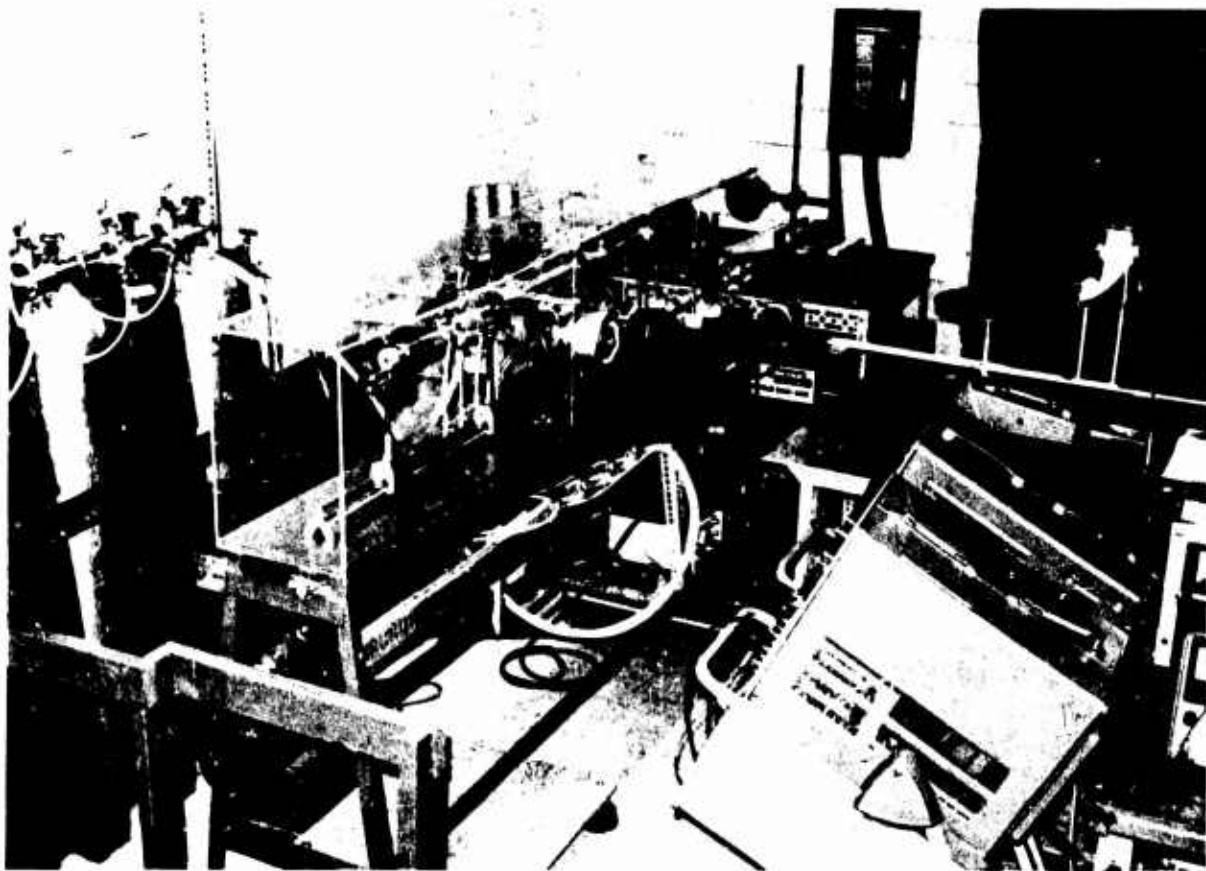


Figure 16b. Photograph of experimental set-up.

lens, and the electronics -- are now described individually.

The CO_2 laser built by the author has a CW output power of 40 watts (11% efficiency). Beam diameter at the output mirror is approximately 1.2 cm (as measured at e-folding points of the power), and divergence is 0.4 mrad. Three gases -- CO_2 at a pressure of 1.4 torr, N_2 at 1.6 torr, and He at 7 torr -- are flowed through the one inch inside diameter pyrex tube. The gold-coated pyrex mirror (diameter 3.81 cm, radius of curvature 10m) and the germanium output mirror (diameter 2.54 cm, flat, 80% reflection) are at a separation of 130 cm. Irtran II windows at the Brewster angle give a vertical polarization at the target surface. The active discharge region is 86 cm in length and is cooled by a concentric water jacket. The output of the power supply (operated at 60ma, 5500v) is filtered to give 0.05% voltage ripple as measured at the discharge tube. The major source of short-term laser noise is the uneven pumping of the Welch fore-pump. Long-term variations are a result of the heating of the mirrors which caused the laser to tune and de-tune itself. Generally the long-term fluctuations stabilize after two hours of operation. Since the precise laser power is not certain, the power is constantly monitored by reflecting part of the beam from an Irtran II flat to a thermopile (Eppley 8-junction Bismuth-Silver). All measurements of scattered power are normalized to the laser power as measured at the thermopile.

The detector is a Santa Barbara Research Corporation gold-doped germanium photoconductive device. All measurements of power were of sufficiently low level that the detector always operated in the linear regime of its bias circuitry. A thin uncoated germanium wafer (transmitting 10%) protects the detector while the coherent component is measured. Also a germanium meniscus lens of diameter 2.5cm and focal length 2.54 cm focuses the radiation onto the detector. Over the face of the lens is a diaphragm which can vary the f/stop from f/1 to f/10 continuously for a more selective sampling of laser power. The lens serves four functions: (a) it increases the signal level at the detector; (b) it increases the signal to noise ratio by filtering the extraneous near-infrared and visible light; (c) it has the effect of reducing the

distance to the far-field; and (d) it performs the surface ensemble average as required by the theory.

The system electronics consist of two oscilloscopes, a lock-in amplifier, two pre-amplifiers, and a chopper wheel. A Tektronix 503 oscilloscope monitors the thermopile voltage. (A micro-voltmeter could be used as well.) The signal from the detector is fed to a PAR 211 pre-amplifier and then to a PAR 120 lock-in amplifier. The pre-amplifier matches the detector to the lock-in amplifier without loading the detector bias circuit, and it allows variable amplification from zero to 60 db. The output of the pre-amplifier is monitored on an oscilloscope for visual inspection of the signal. For a reference signal, a zener diode (detector) views a pilot lamp through the chopper wheel (frequency 330 Hz). That signal is amplified in a Tektronix 1A7A plug-in and fed as a "selective external" input to the lock-in amplifier. The lock-in amplifier is needed to measure the diffuse component of scatter since only the coherent component is easily measured on the oscilloscope. The lock-in amplifier has a time constant set to one second to average the laser short-term fluctuations. This value corresponds to the one second time constant of the thermopile monitoring the beam power.

B. MEASUREMENTS

1. Preliminary Comments.

Measurements were made in the near-field of the surfaces because of the physical difficulties (e.g. alignment) of positioning the detector in the far-field and because of the enhanced signal level in the near-field. (The far-field is for ranges $R_0 \gg 50\text{m}$ for a beam diameter at the surface of 1 cm.) Good agreement for this set-up is expected for the diffuse component of scatter, but not for the coherent component. The coherent scatter is not yet fully developed when the target-to-detector distance is still significant with respect to beam diameter. Most important, in all measurements of scatter (figures 17-20), the coherent component measured is equivalent to the scatter from a perfectly smooth surface replacing the target surface. (On each figure a Gaussian is fitted through coherent data to show where the coherent component

stops and the diffuse starts.) The measurements are not needed to verify the coherent scatter since in part 4 , section F of chapter III we see the reasonability of the theoretical form of coherent scatter.

The measurement is of course power versus θ_2 for θ_1 and θ_3 constants. However, the theory gives power flux (density). A comparison of data with theory is still legitimate provided the size of the detector aperture does not exceed large scale spatial power variations. Small scale variations will be integrated since that average corresponds to the large ensemble average taken in the theoretical derivation. Hence power density curves of theory are compared with experimental power curves by adjusting the ordinate of one with respect to the other. No such adjustment of abscissa is necessary since peaks of coherent components indicate a reference angle.

2. Titanium Scatter.

The data and theoretical curves for scattering from titanium where $\theta_1 = 27^\circ$ are in figure 17 and where $\theta_1 = 3.5^\circ$ in figure 18. General overall agreement is obvious, especially for $|\theta_2 - \theta_1| \leq \pi/4$; however three discrepancies will be accounted for in the order of increasing θ_2 from specular. First, a slight ripple is noted at $\theta_2 \approx 5^\circ$ and 57° in figure 17 and at $\theta_2 \approx 37^\circ$ in figure 18. We can see the source of this seeming anomaly in the power spectrum P_s^t (figures 6 and 8) at $\nu \approx 0.05 \mu^{-1}$. Irregularities of this sort can not be accounted for by the Gaussian model, but they serve the more important role of providing a target signature. A signature is a characteristic of scatter from a surface which is not seen for other surfaces.

Second, for values $|\theta_1 - \theta_2| \geq 40^\circ$ in the roughness component of scatter, the data are higher than theory predicts. The discrepancy is not attributable to any theoretical error because no assumptions are violated until $|\theta_1|$ or $|\theta_2|$ approaches 90° . Moreover such an error does not appear in the aluminum measurements (figure 20). Rather the explanation is that the stylus of the profilometer can not make a perfect trace of the surface but will slightly indent the material. This problem will become worse with

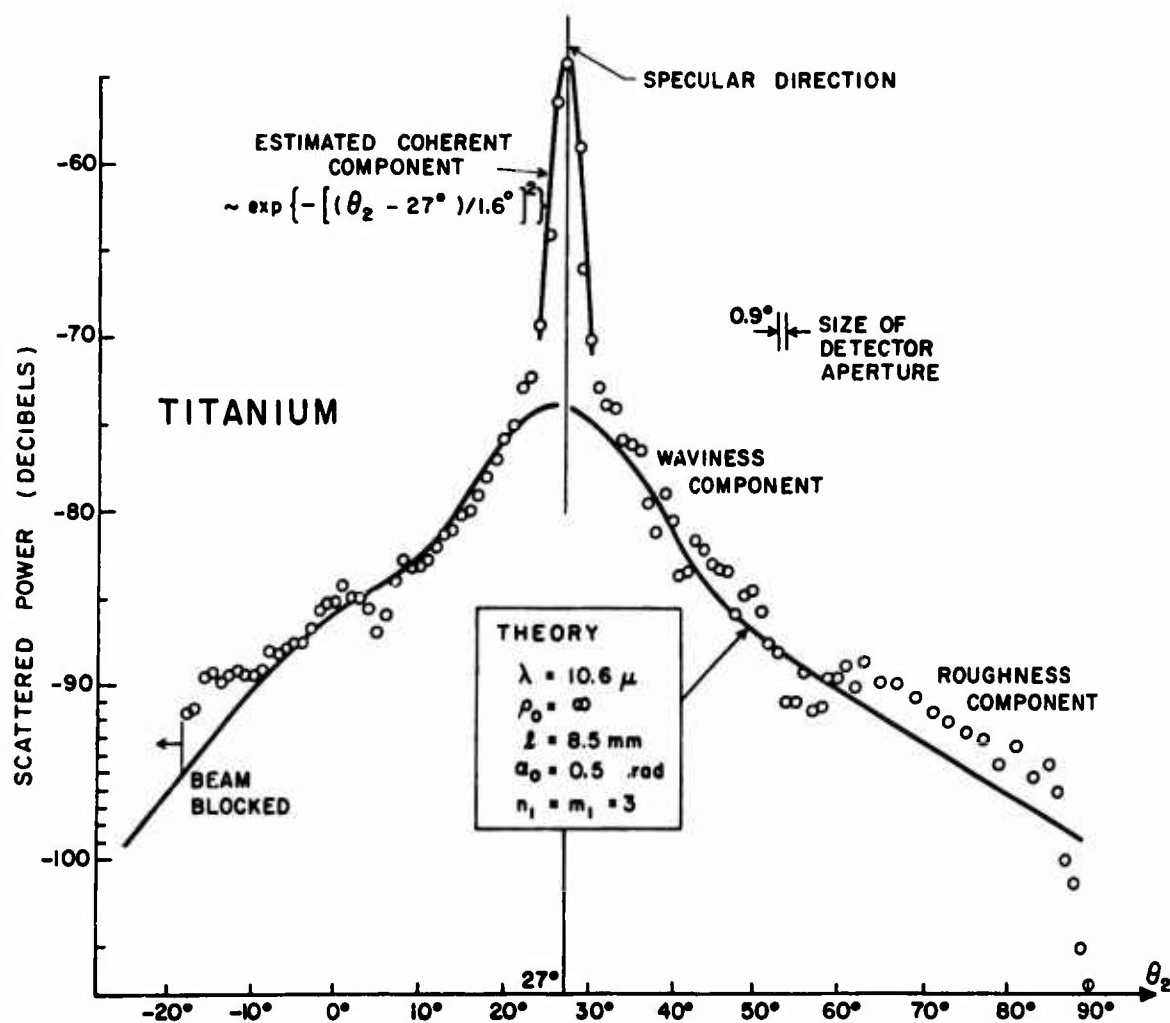


Figure 17. Measured scattered power and theoretical power flux for titanium, $\theta_1 = 27^\circ$, $\theta_3 = 0$. (The vertical scale, in db normalized to backscattered power at vertical incidence, in figures 17-20 is for the theory; ordinate for data is arbitrary.)

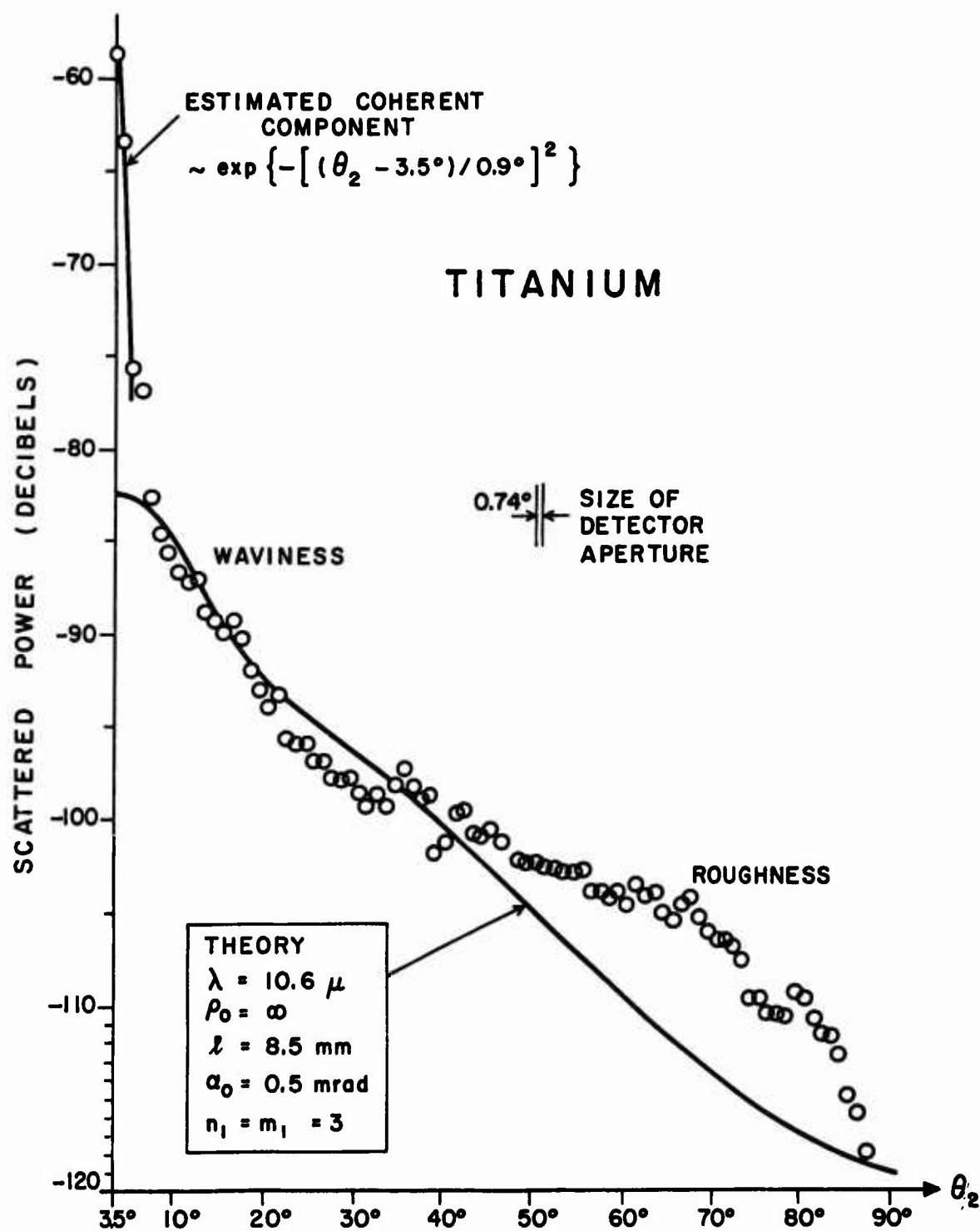


Figure 18. Measured scattered power and theoretical power flux for titanium,
 $\theta_1 = 3.5^\circ$, $\theta_3 = 0$.

increasing wavenumber in the power spectrum. Hence the measured values of $P_s(\nu)$ for $\nu \gg \nu_{NY}/2$ will be lower than is actually the case. This problem is not so bad for aluminum since the aluminum power spectrum is at least a factor of two lower in this large wavenumber region. (See figures 8 and 9.)

Finally, for scatter near the surface edge, the data fall off more rapidly than is predicted. Recall that the theory does not apply for grazing incidence ($|\theta_1| \approx \pi/2$) or grazing scatter ($|\theta_2| \approx \pi/2$). Appendix I analyzes the grazing problem.

3. Aluminum Scatter.

The data and theoretical curves for scatter from the (corroded) aluminum where $\theta_1 = 18^\circ$ are given in figure 19 and where $\theta_1 = 3.5^\circ$ in figure 20. The scatter of figure 19 is especially provided for the waviness component of scatter; whereas figure 20 depicts the excellent agreement in the roughness component. Contrary to titanium measurements, the waviness component does not exhibit good agreement. Initially the modeled values for σ_{s1} and τ_{o1} are suspect. From the data of figure 20 and the procedure of the inverse problem (assuming a Gaussian P_{s1}), we find $\sigma_{s1} = 0.044 \mu$ (rather than the modeled 0.056μ) and $\tau_{o1} = 37.0 \mu$ (rather than the 24.9μ used). (The values are found without a knowledge of the constant A' by assuming the values of σ_{s2} and τ_{o2} are correct and then noting the ratio of the peaks of the individual diffuse components $p_{d1}(0) / p_{d2}(0)$ equals $(\sigma_{s1}\tau_{o1})^2 / (\sigma_{s2}\tau_{o2})^2$.) If the corrected values of σ_{s1} and τ_{o1} were used, the width of the waviness component would be smaller and its peak higher.

In the section presenting surface measurements (chapter III, section A; and figure 7) we saw how traces at different places on the surface give quite different power spectra. The non-stationarity does not significantly affect the scattering behavior provided the beam covers the largest scale surface variations or provided the beam size is so small that the surface under the beam is actually stationary. When scattering from an airplane surface at a large range, the beam diameter will be large enough (about one meter or greater) to average the non-stationarity so that the scattering will

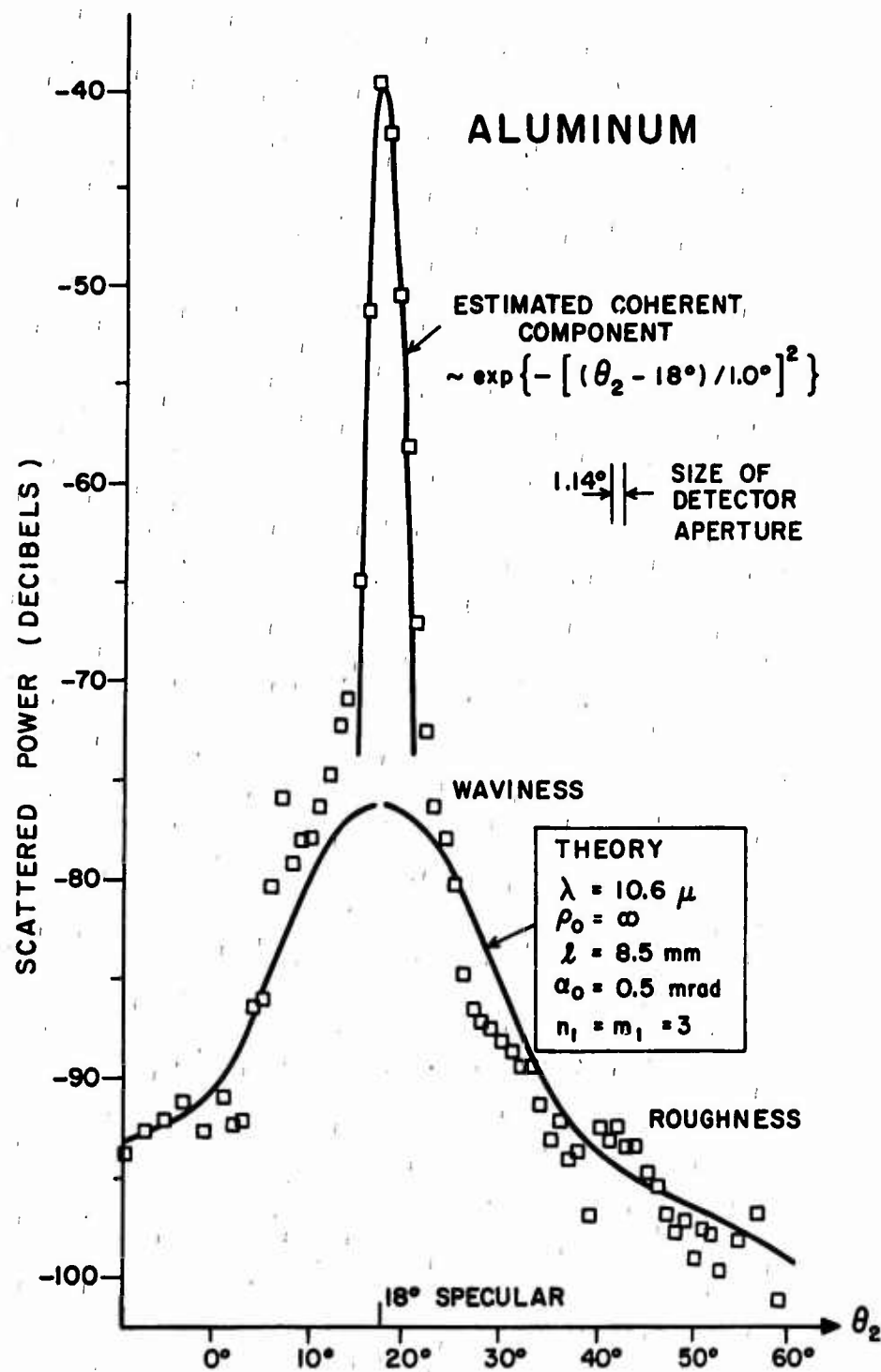


Figure 19. Measured scattered power and theoretical power flux for aluminum,
 $\theta_1 = 18^\circ$, $\theta_3 = 0$.

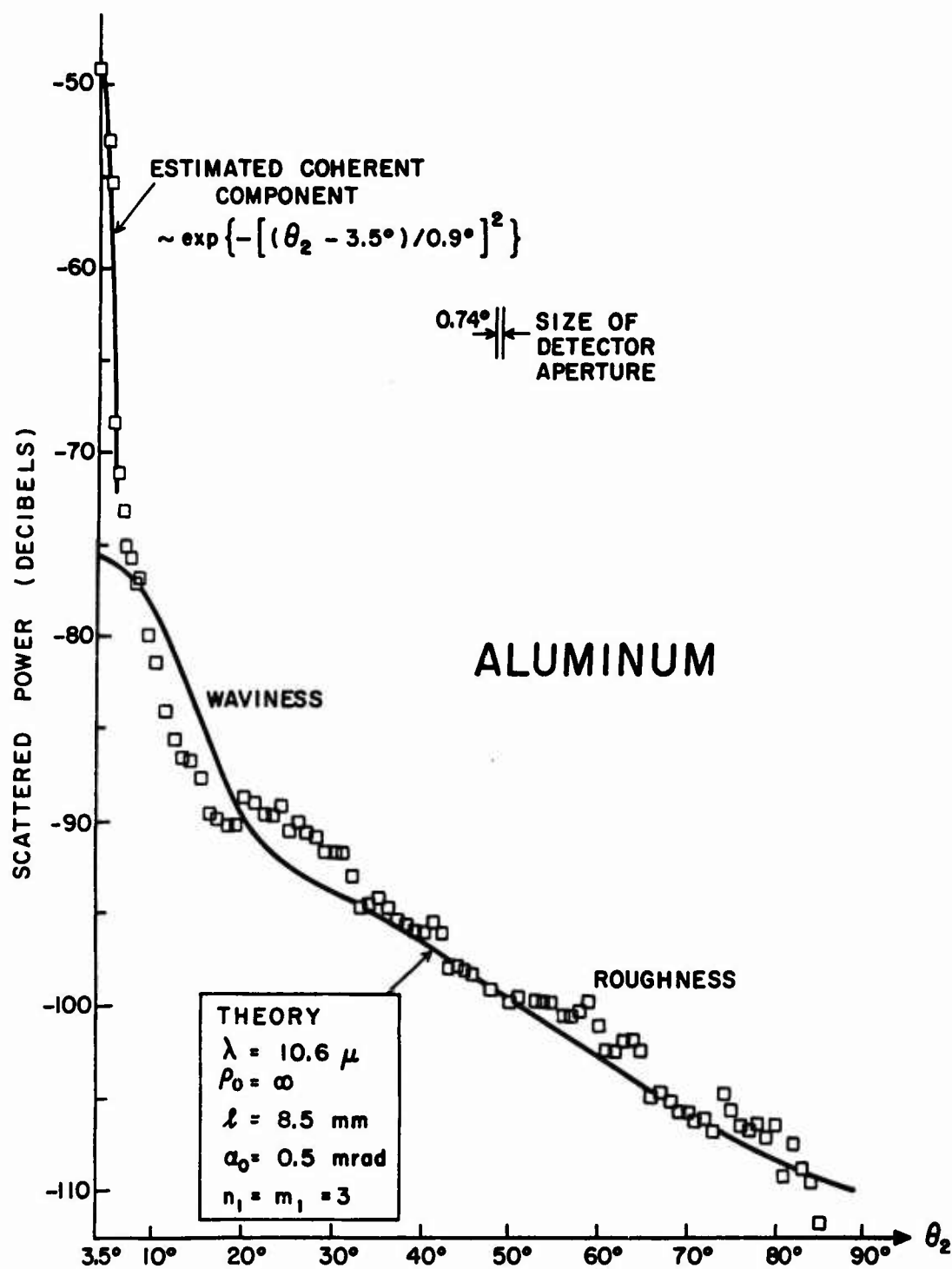


Figure 20. Measured scattered power and theoretical power flux for aluminum, $\theta_1 = 3.5^\circ$, $\theta_3 = 0$.

appear stationary. In the laboratory, the 1 cm beam diameter exposes the non-stationarity of the surface.

4. Titanium Inverse Measurements.

From the data of figure 18, the two-dimensional power spectrum V_s and the one-dimensional power spectrum P_s^S are determined. Since only the diffuse scatter is needed, the first three data points in p_d are estimated. As demonstrated by equation (88), V_s is found by a scaling of p_d . (That spectrum is plotted in figure 21.) After consecutive Bessel and Fourier transforms, P_s^S is found. In figure 22 are P_s^S and P_s^t . Since the proper scaling of p_d is not known (due to the inability to determine p_c in the near-field), there is an arbitrary constant which multiplies P_s^S . Hence the ordinate of P_s^S is adjusted until a good match is obtained with P_s^t . The scale factor would be known if σ_s^2 were measured by some other method. In the laboratory this poses no problem since inexpensive mean-height indicators are generally available. If instead, scatter from an airborne target is measured, the receiver would be in the far-field, and once again the variance would be determined.

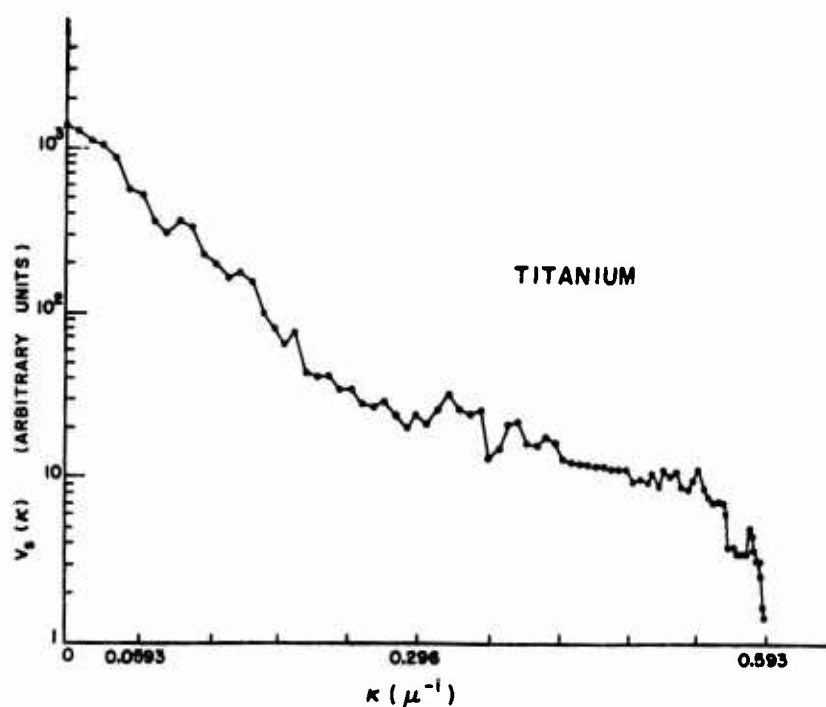


Figure 21. Titanium two-dimensional power spectral density V_s versus wavenumber κ . (Ordinate has units proportional to μ^4 .)

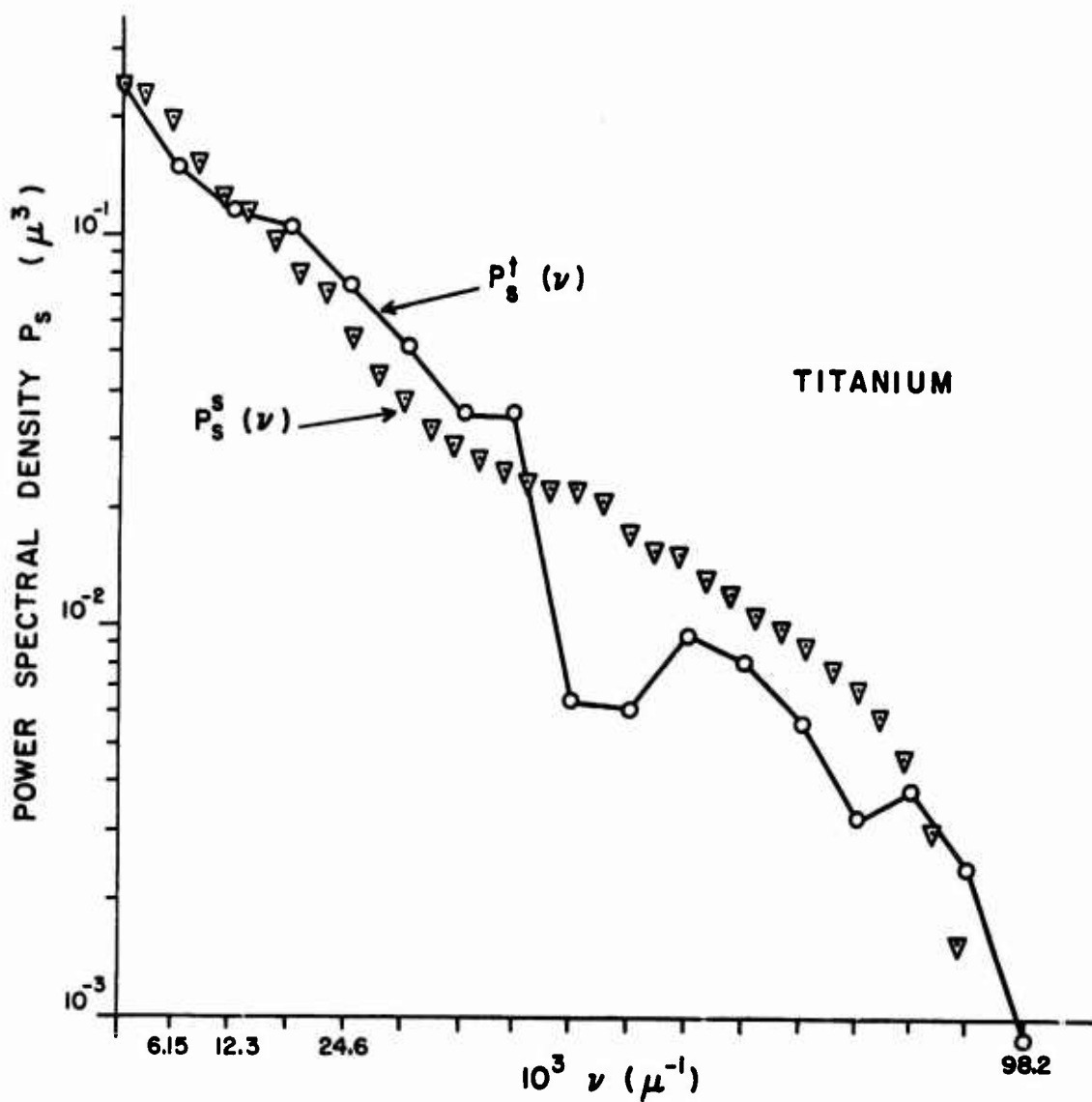


Figure 22. Titanium P_s^t (surface height p.s.d.f. from tracing) and P_s^s (surface p.s.d.f. from scattering). P_s^s is found from the data of figure 18 and the procedure of the inverse problem.

From a comparison of P_S^s and P_S^t , we note the error in the form of $P_S^t(\nu)$ is for frequency ν approaching Nyquist. As noted earlier, the discrepancy is due to the inability of a profilometer to trace small-scale surface variations of significant height accurately. But when the power spectrum is measured by scattering, the surface is not deformed; hence the number of samples (all points under the beam) can be large, and stationarity can be easily verified.

5. Aluminum Inverse Measurements.

The aluminum two and one-dimensional power spectra (figures 23 and 24 respectively) are obtained from the data of figure 20 by the same steps as for titanium. The plot of P_S^s better demonstrates the error in the waviness structure. If the second through fourth points in P_S^t had been used to establish the waviness model, the agreement between scattering theory and data would have been excellent. From an inspection of the individual traces of

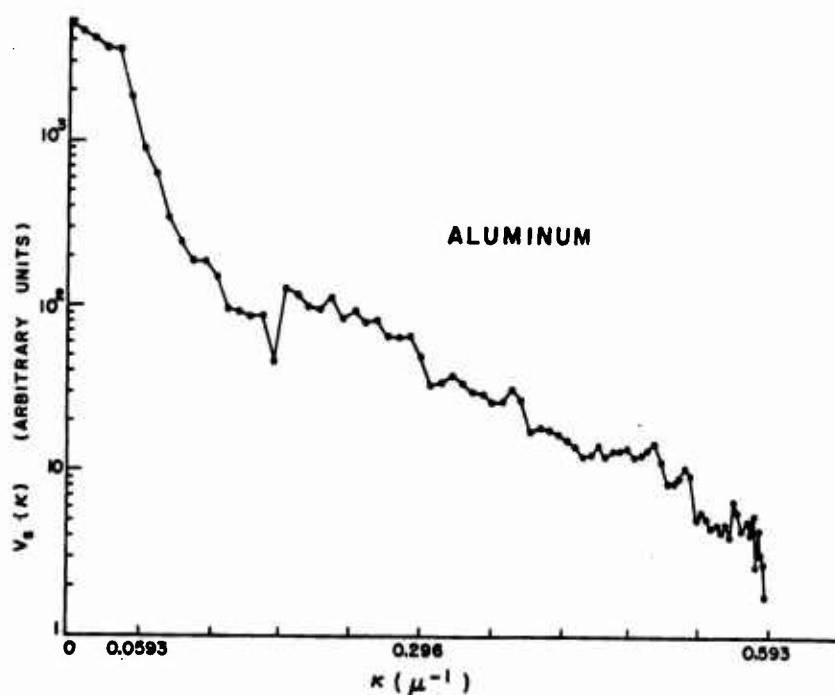


Figure 23. Aluminum two dimensional power spectral density V_s versus wavenumber κ . (Ordinate has units proportional to μ^4 .)

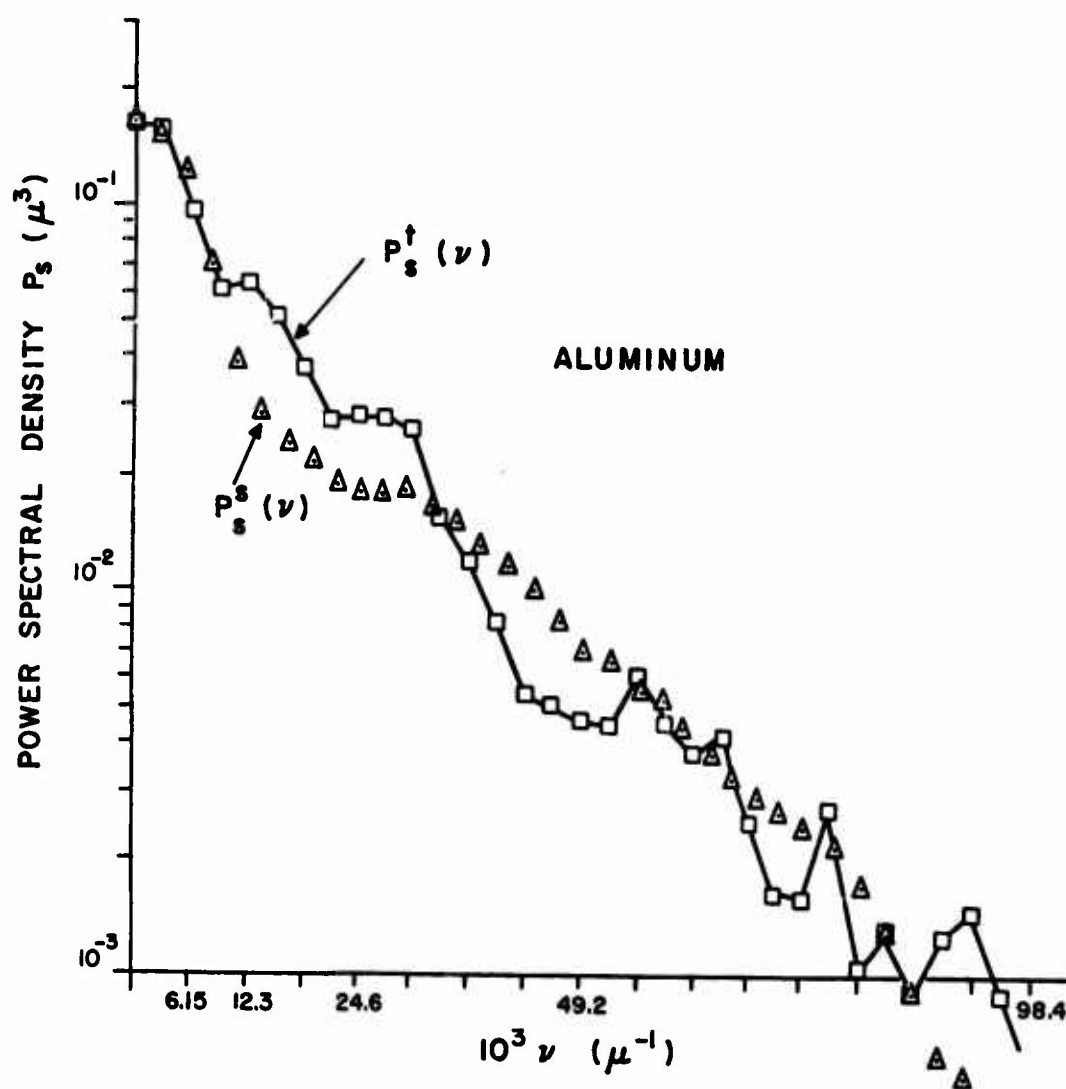


Figure 24. Aluminum P_s^t and P_s^s . P_s^s is found from the data of figure 20 and the procedure of the inverse problem.

P_s^t in figure 7, we see that a single plot (number 3; 13% of all the data) caused the error in waviness component. This indicates that because of the non-stationarity of aluminum, a very large number of samples must be taken to get an average power spectrum.

6. Conclusions.

Taking a two-surface Gaussian model for the surface power spectrum is justified by the form of P_s^s for titanium (figure 22) and for aluminum (figure 24). In those plots, the waviness and roughness components are even more distinct than in the plots of P_s^t . The improvement is of course due to the large number of samples the beam takes when it scatters from an area on the surface. To get a smoother plot of P_s^t , the number of data points should be increased to at least 8000 for aluminum and 2000 for titanium (because of the more-nearly stationary character of the latter). But still the problem of deformation of the surface by the stylus cannot be avoided, and the increased sampling will not help the titanium agreement. To check for surface stationarity, the beam size might be varied and P_s^s found for each size. Conceivably there is a size beyond which the diffuse pattern does not change further. For that size the surface appears stationary, and an average power spectrum is the proper one for use in modeling.

From the scattering measurements already done, we can visualize an optimal system for the determination of rough surface (isotropic, homogeneous) statistics. First the probability density is found on a multi-channel analyzer (MCA) by evaluation of the proficorder output. If the density is nearly Gaussian and isotropic, then the theoretical derivation of the inverse problem is appropriate. Since a proficorder is being used, the surface variance, σ_s^2 , is easily measured -- either from the meter on the proficorder or as the second central moment of the probability density. Next the appropriate laser is chosen for scattering, depending on what Nyquist frequency (λ^{-1}) is desired. The beam is to have an incident angle as near normal as possible. The scattered pattern from specular to the edge is measured and fed to a computer program

which scales and transforms to get P_s^S . Final scaling of P_s^S is done with the σ_s^2 found by another method. Finally, from the knowledge of P_s , one might filter the proficorder output into waviness and roughness components for individual analysis on the MCA. The advantage of this system over recording the trace and analog-to-digital converting is in time saving. An excessive number of data points must be used to properly establish the power spectra via tracing, but only about 90 to 180 data samples are taken in scattering. If the cost of the MCA and proficorder is prohibitive, then the investigator might establish the probability density by theoretical considerations (central limit theorem) and measure σ_s^2 on a simple (inexpensive) roughness-measuring device. In any case, the computer is only used for data reduction, and the problem of analog-to-digital conversion is avoided.

Chapter V

CONCLUSIONS

With the increasing development and use of new airplane surfaces (such as Graphite/Epoxy and Boron/Epoxy), measurements of scattering and the establishment of new models will need to be effected for the new surfaces. Also one surface presently in use, the painted one, needs to be modeled by persons who have the material available to them. Since additional information is available on the surface when the wavelength is changed, scattering measurements should be made at wavelengths shorter than the 10.6μ used in this analysis. (As pointed out in the text, the aluminum and titanium surfaces are moderately rough at 1.0μ ; hence the theory should still give good agreement there.) For all surfaces examined, the power spectra and scattering curves should be carefully inspected for unique characteristics which will be useful in target identification. Such a characteristic was found for titanium as a "ripple" in the power spectrum.

The theory (in the form of equation (66)) is now ready for the generation on a digital computer of simulated target images. The target would be described by grid-points in a three-dimensional space, where the spacing of grid lines is less than the beam diameter. A quadric surface would approximate the deterministic surface at each grid crossing, and the scatter to the detector at some bistatic or monostatic angle would be calculated. The assemblage of the returns constitutes the image. Then the techniques of pattern recognition would be applied to help establish a target-image relationship. At the same time laboratory measurements of target images will further establish the relation.

Turbulence was carefully injected into the scattering problem because a disturbance of the incident plane wave character will obviously affect the scattering. However, scintillation of the beam on the return path is not an integral part of the scattering and hence must be treated separately. Once again the optical transfer function would be used but would be applied to the total target image in the image coordinate system. The optical transfer

function derived in the text is not limited to use in this scattering problem. The atmospheric OTF is important in all problems of propagating a coherent beam through a turbulent medium. The result will find uses in communications and radar.

Finally, the reader should be especially aware of the transfer function formulation which allows the investigator to vary some aspects of the problem without disturbing the rest. The solution was kept as general as possible before applying it to laser scattering from rough metallic surfaces so that the solution can be easily applied to other scattering problems, including underwater scattering from targets and scattering from the ocean surface.

APPENDIX I

Verification of Inequalities (11) and (18)

This appendix presents more explicit inequalities to replace (11) and (18) based on the chosen field profile and OTF of chapter III. Neither inequality can be strictly satisfied since U is a stochastic quantity which can go to zero. However, the replacement yields inequalities not so precise but easier to use.

For an isotropic homogeneous random variable with Gaussian autocorrelation, the standard deviation (σ') of the derivative of the variable is given by

$$\sigma' = \sqrt{2} \sigma / T_0 \quad (106)$$

where σ is the standard deviation of the variable, and T_0 is the e-folding distance of the autocorrelation. Also the following replacement is used:

$$\frac{U_r}{U} = (w + i \varphi)_r + \frac{e_r}{e} \quad (107)$$

$$\text{where } w = \ln |Z| \text{ and } \varphi = \arg(Z) \quad (108)$$

represent the random nature of the medium, and the sub-r indicates the x, y or z partial derivative. Using (107), each inequality is split into a "deterministic" and a "statistical" inequality. From (106), the approximations

$$\begin{aligned} |(w + i \varphi)_x| &\leq (\cos \theta_1) \sqrt{2} / \rho_0, \\ |(w + i \varphi)_y| &\leq \sqrt{2} / \rho_0, \\ |(w + i \varphi)_z| &\leq |\sin \theta_1| \sqrt{2} / \rho_0 \end{aligned} \quad (109)$$

are made. (Note the variance of $(w + i \varphi)$ is $B_u(0)$, and $T_0 = 0.945 L_0 [B_u(0)]^{-1/8}$.) In a similar fashion:

$$\begin{aligned} \left| \frac{e_x}{e} \right| &\leq (\cos \theta_1) 2/\ell, \\ \left| \frac{e_y}{e} \right| &\leq 2/\ell, \end{aligned}$$

and
$$\left| \frac{e_z}{e} \right| \leq |\sin \theta_1| 2/l. \quad (110)$$

Using (107), (109), and (110), the first inequality (11) decouples into a "deterministic" inequality

$$\frac{2}{kl} |\tan \theta_1| \ll 1 \quad (111)$$

and a "statistical" inequality

$$\frac{\sqrt{2}}{k \rho_0} |\tan \theta_1| \ll 1. \quad (112)$$

Inequality (18) weakens when $\theta_3 = 0$ and $\theta_2 = \theta_1 \approx \pm \pi/2$ (specular scatter near grazing). For these angles, (18) becomes

$$\frac{2}{kl} \sec^2 \theta_1 \ll 1 \quad (113)$$

and
$$\frac{\sqrt{2}}{k \rho_0} \sec^2 \theta_1 \ll 1. \quad (114)$$

In summary, the four inequalities (111-114) depend only on the wavelength, the incident angle, and the e-folding lengths of the OTF and the incident field. The inequalities say the work of this paper is not applicable to the study of scattering for grazing incidence. Finally, use of the weak bounds of (109) and (110) is justified in that the inequalities are indeed easily satisfied. If the inequalities had turned out to be marginal, then a more precise replacement would have been necessary.

APPENDIX II

Integration for the Wave Correlation Function

This section briefly outlines the steps taken in arriving at the approximate form (55) for the wave correlation function. Initially the integral (52) which defines the correlation is rewritten as

$$C_u(\rho') \sim \int_0^{\kappa_m L_0} J_0(\kappa' \rho') (1 + \kappa'^2)^{-11/6} \kappa' d\kappa' \quad (115)$$

(where $\rho' = \rho/L_0$, and $\kappa' = \kappa L_0$) to reduce the number of parameters from two (κ_m and L_0) to one ($\kappa_m L_0$). Equation(115) was numerically integrated using the rectangular rule on a digital computer. It was normalized such that $C_u(\rho')$ at some small ρ' (less than $1/(\kappa_m L_0)$ but not zero) matches the value for $C_u(\rho')$ as given by (54). Next the function

$$y = -\ln C_u(\rho') \quad (116)$$

was plotted on log-log paper in order to determine the parametric dependence and possible functional dependence (perhaps $C_u \sim \exp(-b \rho'^a)$, b and a constants). That plot (of which a significant portion is in figure 25) demonstrates the exponent, a , decreases from 2.0 to 1.5 as ρ' increases from 10^{-4} to 10^{-1} . However, a Gaussian form for C_u is desired; hence a suitable method of approximating $a \approx 2$ is presented. Since form (54) is essentially valid for $\rho' < 1/(\kappa_m L_0)$, the following curve (117) is also plotted (the dashed line) as an upper boundary for the validity of (54):

$$y_1(\rho') = \frac{5}{4} [(\rho')^{-1/3} - \frac{6}{5}] (\rho')^2. \quad (117)$$

Then

$$y_1(\rho') \approx 0.695 (\rho')^{8/5}, \quad 10^{-5} < \rho' < 10^{-1}, \quad (118)$$

is found as a graphical approximation to (117). Fortunately for a constant $B_u(0)$ and the OTF C_0 varying from 0.9 to 0.1, the function $y = -\ln(C_u)$

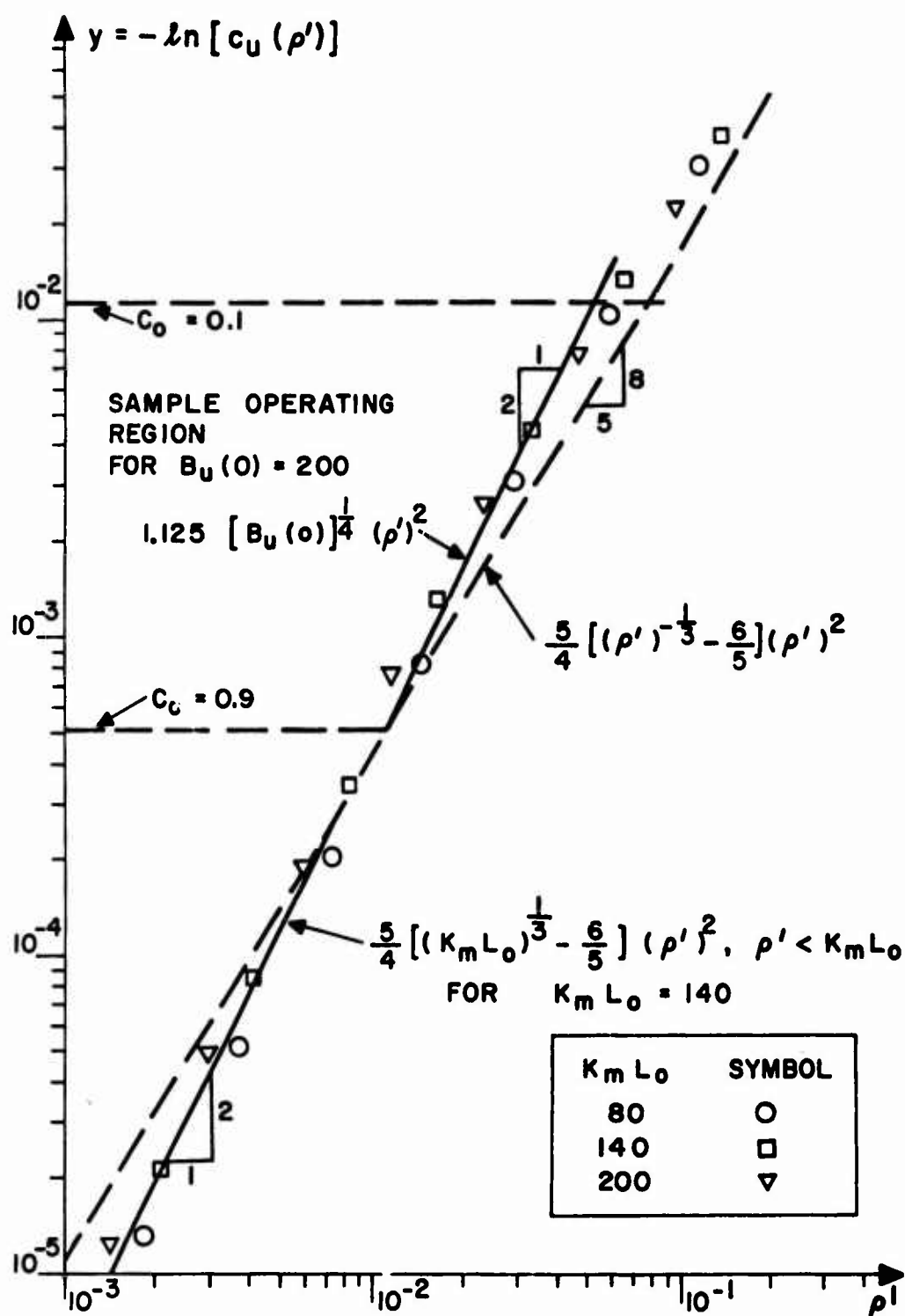


Figure 25. Plot used in determining the approximate Gaussian form for the OTF. (Symbols correspond to computer generated data. See appendix II.)

varies only slightly more than one decade. (For a given C_o , say 0.9 or 0.1, the ordinate is

$$y_o \approx \frac{|\ln C_o|}{B_u(0)} . \quad (119)$$

Then note $\ln(0.1) / \ln(0.9) = 22.$ Over this decade (termed the "operating region"), the following approximate form is used:

$$y = \delta_2 (\rho')^2 . \quad (120)$$

The constant δ_2 is found by forcing the curve (120) to intersect the dashed line (118) at $y = y_o$ where $C_o = 0.9$. (The C_o was chosen by trial and error to get the quadratic y in (120) as close as possible to the numerical results within the operating region.) Namely $y_1 = y_o$ in (118) determines the abscissa ρ' of the intercept. Finally $y = y_1$ and the ρ' thus determined are substituted in (120) to yield

$$\delta_2 = 1.125 (B_u(0))^{1/4} . \quad (121)$$

All that remains is to write the wave correlation as (55) using (116), (120), and (121). Equation (55) is said to be the appropriate one if ρ' at the intercept is greater than $1/(\kappa_m L_o)$:

$$\kappa_m L_o \geq 3.3 (B_u(0))^{5/8} . \quad (122)$$

If (122) is not satisfied, then the form (54) is to be used.

APPENDIX III

Relations Between n-dimensional Power Spectra

This section provides the mathematical relations between power spectral densities in one, two, and three dimensions. If an n-dimensional random field is isotropic and homogeneous, then a one-dimensional sample of the field is sufficient to give the power spectrum in any dimension ($\leq n$). Some of the results of this appendix are used by the inverse problem of chapter III section G.

The basis for the relations is that the (homogeneous but not-necessarily isotropic) covariance $B(\bar{\Delta})$ is invariant with dimension in that it is the (1,1) moment of the joint probability density $W(z_1, z_2; \bar{\Delta})$:

$$B(\bar{\Delta}) = \int_{-\infty}^{\infty} \int_{-\infty}^{\infty} z_1 z_2 W(z_1, z_2; \bar{\Delta}) dz_1 dz_2 . \quad (123)$$

However, the power spectrum $V^{(n)}$ (where n is the dimension) is the n-th order Fourier transform of $B(\bar{\Delta})$:

$$V^{(n)}(\bar{\kappa}) = \int_{-\infty}^{\infty} \dots \int_{-\infty}^{\infty} B(\bar{\Delta}) e^{-i \bar{\kappa} \cdot \bar{\Delta}} d\bar{\Delta} \quad (124)$$

where $\bar{\kappa} = (\kappa_1, \kappa_2, \dots, \kappa_n)$, $\bar{\Delta} = (\Delta_1, \Delta_2, \dots, \Delta_n)$, and $d\bar{\Delta} = d\Delta_1 d\Delta_2 \dots d\Delta_n$. If isotropy is assumed:

$$B(\bar{\Delta}) = B(\rho) \quad (125)$$

where $\rho = |\bar{\Delta}|$, and the Fourier transform (124) may be reduced to a one-dimensional integral. In particular, the relations for $n=1, 2, 3$ are:

$$B(\rho) = \frac{1}{\pi} \int_0^{\infty} \cos(\kappa \rho) V^{(1)}(\kappa) d\kappa \quad (126)$$

$$= \int_0^{\infty} J_0(\kappa \rho) V^{(2)}(\kappa) \kappa d\kappa \quad (127)$$

$$= \frac{2}{\rho} \int_0^{\infty} \sin(\kappa \rho) V^{(3)}(\kappa) \kappa d\kappa \quad (128)$$

where $\kappa = |\bar{\kappa}|$. Since the three transforms possess inverses, they provide a means of going between power spectral densities of dimension $n \leq 3$.

In some cases, more direct expressions which relate $V^{(n)}(\kappa)$ may be written from (126 - 128). First,

$$V^{(3)}(\kappa) = - \frac{1}{\kappa} \frac{\partial V^{(1)}}{\partial \kappa} \quad (129)$$

is found by substituting (128) into the inverse of (126), and then taking the derivative with respect to κ . (Tatarski [3] found the same result by an alternate method.) Second, a power spectrum in a particular dimension is related to the spectrum in the next lower dimension by

$$V^{(n-1)}(\kappa) = \int_{\kappa}^{\infty} \frac{2 \kappa'}{\sqrt{\kappa'^2 - \kappa^2}} V^{(n)}(\kappa') d\kappa' \quad (130)$$

(provided $V^{(n)}$ is Bessel-transformable). Unfortunately a transform inverse to (130) which is a one-dimensional integral does not exist. Hence to go from $V^{(n)}$ to $V^{(n+1)}$, the transforms in (126-128) and their inverses must be used. Those transforms are in fact easier to use than (130) since Fourier integral tables are available.

REFERENCES

- [1] P. Beckmann and A. Spizzichino, The Scattering of Electromagnetic Waves from Rough Surfaces. New York: Macmillan, 1963.
- [2] C. Eckart, "The Scattering of Sound from the Sea Surface," J. Acoust. Soc. Am., vol. 25, pp. 566-570, May 1953.
- [3] V. I. Tatarski, Wave Propagation in a Turbulent Medium. New York: McGraw-Hill, 1961.
- [4] J. W. Strohbehn, "Line-of-Sight Wave Propagation Through the Turbulent Atmosphere," Proc. IEEE, vol. 56, pp. 1301-1318, August 1968.
- [5] I. Stakgold, Boundary Value Problems of Mathematical Physics, Vol. II. New York: Macmillan, Sect. 7.15, 1967.
- [6] J. C. Leader, "Multiple Scattering of Electromagnetic Waves from Rough Surfaces," presented at the Fall Meeting of the OSA, Hollywood, Florida, 28 Sept. - 20 Oct. 1970.
- [7] G. R. Valenzuela, "Depolarization of EM Waves by Slightly Rough Surfaces," IEEE Trans. on Antennas and Propagation, vol. AP-15, pp. 552-557, July 1967.
- [8] J.B.P. Williamson, J. Pullen, and R. T. Hunt, "The Shape of Solid Surfaces," Surface Mechanics: ASME Winter Annual Meeting, Los Angeles, California, November 16-21, 1969.
- [9] J. B. P. Williamson, "Microtopography of Surfaces," Proc. Instn. Mech. Engrs., vol 182, pt. 3K, pp. 21-30, 1967-8.
- [10] G. M. Jenkins and D. G. Watts, Spectral Analysis and Its Applications. San Francisco: Holden-Day, p. 64, 1969.
- [11] R. B. Blackman and J. W. Tukey, The Measurement of Power Spectra. New York: Dover, p. 22, 1958.

- [12] R. E. Hufnagel and N. R. Stanley, "Modulation Transfer Function Associated with Image Transmission through Turbulent Media," J. Opt. Soc. Am., vol. 54, pp. 52-61, January 1964.
- [13] M. J. Beran, "Propagation of the Mutual Coherence Function through Random Media," J. Opt. Soc. Am., vol. 56, pp. 1475-1480, November 1966.
- [14] M. J. Beran, "Comments on 'Line-of-Sight Wave Propagation Through the Turbulent Atmosphere'," Proc. IEEE, vol. 57, p. 703, April 1969.
- [15] J. W. Strohbehn, "Comments on 'Line-of-Sight Wave Propagation Through the Turbulent Atmosphere', Author's Reply," Proc. IEEE, vol. 57, pp. 703-704, April 1969.
- [16] W. P. Brown, "Validity of the Rytov Approximation," J. Opt. Soc. Am., vol. 57, pp. 1539-1543, December 1967.
- [17] D. L. Fried, G. E. Meyers, and M. P. Keister, "Measurements of Laser Beam Scintillation in the Atmosphere," J. Opt. Soc. Am., vol. 57, pp. 787-797, 1967.
- [18] S. F. Clifford, G. M. B. Bouricius, and G. R. Ochs, "Phase Variations in Atmospheric Laser Propagation," Environmental Research Laboratories, Wave Propagation Laboratory, Boulder, Colorado 80302.
- [19] H. T. Yura, "Small-Angle Scattering of Light by Ocean Water," Appl. Opt., vol. 10, pp. 114-118, January 1971.
- [20] A. M. Whitman and M. J. Beran, "Beam Spread of Laser Light Propagating in a Random Medium," J. Opt. Soc. Am., vol. 60, pp. 1595-1602, December 1970.